PCCP

ROYAL SOCIETY OF CHEMISTRY

PAPER

View Article Online
View Journal | View Issue

Cite this: *Phys. Chem. Chem. Phys.*, 2025, **27**, 7773

Electrocatalytic reduction of nitrogen to ammonia on metal nanoclusters: insights and trends from d- and p-block metals†

Rajesh Kumar Raju [ab]

The electrocatalytic reduction of nitrogen (NRR) to ammonia on metal nanoclusters represents a transformative approach to sustainable ammonia synthesis, offering a greener alternative to the highly energy-intensive Haber–Bosch process, which is a significant contributor to global CO_2 emissions. By harnessing renewable electricity under ambient conditions, electrocatalytic NRR could dramatically lower the carbon footprint and enable decentralized, on-demand ammonia production. However, the inherent stability of N_2 presents a major obstacle to its efficient activation. Metal nanoclusters, with their distinctive electronic and structural characteristics, have emerged as highly promising catalysts to overcome this challenge. This study systematically investigates the NRR catalytic performance of a broad spectrum of d-block and p-block metal nanoclusters. Through the use of Genetic Algorithms (GA) for global minimum structure optimization and comprehensive mechanistic pathway analysis, we uncover key trends in N_2 activation, NRR reaction pathways, selectivity, and efficiency across various nanoclusters. Our findings provide critical insights into the design of advanced NRR electrocatalysts, paving the way for more sustainable and efficient technologies for ammonia production.

Received 5th January 2025,
Accepted 24th March 2025

DOI: 10.1039/d5cp00046g

rsc.li/pccp

Introduction

The catalytic reduction of nitrogen (N_2) to ammonia (NH_3) is of immense significance for both industrial applications and environmental sustainability.[1–5] Ammonia is a crucial component in fertilizer production, playing an indispensable role in global agriculture and food security. However, the conventional method for synthesizing NH_3, the Haber–Bosch process, is highly energy-intensive and heavily reliant on fossil fuels, leading to substantial CO_2 emissions.[1–5] As the world moves toward greener and more sustainable technologies, developing efficient and environmentally friendly alternatives to the Haber–Bosch process has become a critical scientific and technological goal.

Electrocatalytic nitrogen reduction reaction (NRR) presents a promising alternative for sustainable ammonia production by utilizing renewable electricity to drive the conversion of N_2 to NH_3 under ambient conditions.[6–9] This approach has the potential not only to reduce the carbon footprint of ammonia production but also to enable decentralized and on-demand synthesis, which could transform the fertilizer industry and related sectors. However, achieving practical and efficient ammonia synthesis through electrocatalytic NRR is challenging due to several formidable obstacles.

One of the main challenges is the activation of the highly stable N_2 molecule, which possesses a triple bond with a dissociation energy of 941 kJ mol^{-1}, making it difficult to break.[10] Additionally, the NRR competes with the hydrogen evolution reaction (HER), which often dominates under electrochemical conditions, reducing the selectivity and yield of NH_3. The low solubility of N_2 in aqueous electrolytes and the difficulty of efficient electron transfer to N_2 further complicate the process.

[a] *National Research Council Canada, Clean Energy Innovation (CEI) Research Centre, Mississauga, Ontario L5K 1B4, UK. E-mail: rajesh.raju@nrc-cnrc.gc.ca, rajesh444@gmail.com*
[b] *School of Chemistry, University of Birmingham, Birmingham B15 2TT, UK*

† Electronic supplementary information (ESI) available: The ESI includes several figures and tables providing detailed insights into the nitrogen reduction reaction (NRR) on various metal nanoclusters. Fig. S1 presents residual Bader charges for different NRR adsorbates across 3d, 4d, 5d, and p-block metals, Fig. S2 illustrates the correlation between adsorption free energies (ΔG) and residual Bader charges for these adsorbates, excluding p-block and pseudo-p-block metals. Fig. S3 reports the HOMO–LUMO gaps for NRR adsorbates, and Fig. S4 and S5 show correlation plots for the adsorption free energies of N* and N_2* with other intermediates. Table S1 summarizes the bond distances between nitrogen and metal atoms in the global minimum configurations of nanoclusters, reporting the shortest bond when two nitrogen atoms are involved in bonding and Table S2 provides N–N bond distances in adsorbates. Table S3 presents adsorption free energies (ΔG) for various NRR intermediates. Table S4 lists residual Bader charge values, and Table S5 reports spin multiplicities for intermediates and global minimum configurations. Table S6 details the HOMO–LUMO gaps, and Table S7 outlines the thermodynamic free energy changes for different electrochemical steps in the NRR. See DOI: https://doi.org/10.1039/d5cp00046g

Nanoclusters have emerged as a particularly promising class of materials for addressing these challenges in electrocatalytic NRR.[11–20] These nanoclusters, characterized by their distinct electronic, optical, magnetic, and chemical properties, offer significant advantages over bulk materials and larger nanoparticles due to their exceptional surface-to-volume ratio and unique electronic structures.[21–26] Nanoclusters typically composed of a few to a few hundred metal atoms and are extremely monodispersed small nanoparticles with atomic precision, exhibit a transition from the bulk to molecular regions. The catalytic behavior of nanoclusters can be finely tuned by controlling their size, shape, and composition, providing opportunities to enhance NRR activity and selectivity. Moreover, nanoalloys, or alloy nanoclusters, have garnered significant interest in nanocatalysis, offering catalytic properties that differ markedly from those of pure metal nanoclusters.[27–32] The synergistic effects arising from the combination of different metals in nanoalloys can lead to improved N_2 activation, stabilization of key intermediates, and suppression of competing reactions like HER.

Studies have shown the efficiency of various nanocluster systems including nanoalloys for NRR.[33] Jiang *et al.* highlighted that low-coordinate atoms in amorphous Ru nanoclusters improve ammonia yield and faradaic efficiency and outperforming their crystalline counterparts.[34] Han *et al.* demonstrated that Ni doping in Ag_4Ni_2 nanoclusters enhanced performance by suppressing HER and enabling charge reconstruction.[35] Ding *et al.* emphasized the activity of Ru-doped CeO_2 nanorods due to oxygen vacancies providing active N_2 adsorption sites.[36] Tan *et al.* reported that Mo-decorated Au_{25} nanoclusters improved catalytic activity for NH_3 production.[37] Shi *et al.* showed that optimizing the $Pd_{0.2}Cu_{0.8}$ alloy composition on graphene boosted NRR performance.[38] Ahmed *et al.* demonstrated synergistic effects of $CoFe_2O_4$ clusters on graphene, enhancing ammonia synthesis.[39] Suryanto *et al.* revealed that Ru nanoclusters on 2H-MoS_2 suppressed HER and improved NRR selectivity.[40] Catalysts such as RhP_x nanoparticles[41] embedded in N, P dual-doped carbon films and Rh_2Sb nanorods[42] with rough surfaces have shown significant improvements in NRR. Surface-modified systems like Pd nanoparticles with tannic acid[43] and Cu nanoparticles supported on TiO_2[44] with oxygen vacancies have leveraged metal–support interactions for better catalytic activity. High-entropy alloys, such as RuFeCoNiCu[45] nanoparticles with small size alongside bimetallic systems like $FeWS_x$@$FeWO_4$,[46] and $NbTiO_4$ nanoparticles supported on nitrogen-doped carbon nanorods,[47] have also emerged as highly effective catalysts. Additional systems, including ultrafine Rh nanoparticles on CNT,[48] Au nanoparticles anchored on a MOF,[49] carbon–supported Pt–Rh nanoparticles,[50] Ru-based Heusler alloys,[51] Au@$Cu_{2-x}Se$,[52] and V_2O_3/VN[53] further highlight the broad potential of nanocluster and alloy catalysts in advancing NRR efficiency through targeted structural and electronic modifications.

Modeling plays a pivotal role in designing and optimizing nanoclusters for nitrogen reduction reaction (NRR), enabling researchers to predict and refine the electronic structure and surface properties of these materials to achieve optimal catalytic performance. While most prior density functional theory (DFT) studies have focused on NRR catalysis over metal surfaces or metal-oxide surfaces, investigations into nanocluster catalysts remain relatively limited.[33,54–59] When nanoclusters have been studied, they are often restricted to a specific metal or a small subset of metals.[57,60–62] Additionally, many of these studies rely on known crystal surface lattices to model nanoclusters, often overlooking the possibility that the true global minimum (GM) configurations of nanoclusters, including adsorbate-bound ones, may differ significantly from bulk geometries. Given the vast number of possible nanocluster configurations with near-identical energies, accurately identifying the GM for each nanocluster is crucial to properly assess its catalytic behavior.

A significant challenge arises when NRR intermediates or other adsorbates form on the nanocluster surface, as these interactions can dramatically alter the electronic and geometric properties, leading to reorganization or rearrangement of nanocluster moiety. This reconfiguration can shift the nanocluster towards a new, stable minimum, which may drastically impact the overall energetics and reaction pathways. Therefore, determining the correct geometry for both pristine and adsorbate-bound nanoclusters is essential for accurately predicting catalytic performance and optimizing nanoclusters for NRR.

In this study, we introduce a novel approach that combines global minimum structure searching, using genetic algorithms (GA),[63–65] with electrochemical studies of NRR on a wide range of metal nanoclusters. The GA-driven search explores the vast configurational space of nanoclusters, allowing us to identify the most stable structures and their corresponding energetics under realistic catalytic conditions. This is particularly critical since the adsorption and interaction of nitrogen intermediates can dramatically alter the structural and electronic properties of nanoclusters, and understanding these changes is essential for accurate predictions of catalytic performance. By coupling GA-based structure optimization with detailed electrochemical analyses of reaction intermediates and pathways, our work provides a comprehensive view of how nanoclusters behave in NRR. This allows for the identification of catalytically favorable nanocluster configurations that were previously overlooked, offering new insights into improving catalytic efficiency in nitrogen fixation reactions.

This study provides a systematic evaluation of size-selected 10-atom nanoclusters for NRR, encompassing all transition metals (d-block) from the 3d, 4d, and 5d series, as well as selected p-block metals, including Al, Ga, In, Tl, Sn, Pb, and Bi. The deliberate inclusion of p-block metals alongside d-block metals introduces a novel dimension to NRR studies. Transition metals are well-recognized for their partially filled d-orbitals, which facilitate the activation of N_2 through π-back-donation, while p-block metals, with their unique electronic and geometric properties, offer complementary pathways for stabilizing intermediates and modulating reaction mechanisms. This expanded scope addresses a critical gap in the literature, where studies on nanocluster catalysts are often limited to a few metals or bulk-like configurations.

While s-block and f-block metals were excluded, this decision was guided by their limited catalytic relevance to NRR. s-block metals, lacking d-orbitals, exhibit weak binding with N_2 and intermediates, while f-block metals, though theoretically intriguing, pose challenges due to their complex electronic configurations and limited practical applications in NRR catalysis. Prioritizing d-block and p-block metals allows for a focused evaluation of elements with the highest potential for catalytic activity.

Unlike most previous studies that focus on bulk surfaces or limited subsets of metals, this work systematically evaluates a broad spectrum of metal nanoclusters, uncovering catalytic trends that were previously unexplored. In addition to structural optimization, this study advances the field by performing detailed mechanistic pathway analyses, including adsorption free energies, charge transfer dynamics, and potential-determining steps. The inclusion of linear scaling relationships and descriptor-based analyses provides actionable insights for rational catalyst design, offering a framework for optimizing nanocluster catalysts.

The study also adopts a rigorous computational methodology to ensure the accuracy of results. Global minimum configurations for both pristine and adsorbate-bound nanoclusters were identified using a well-established Genetic Algorithm (GA). This approach overcomes the limitations of previous studies that often rely on assumed geometries derived from bulk surfaces, which may not represent the true energetics of nanocluster systems. By systematically determining the most stable configurations, we provide a robust foundation for analyzing catalytic behavior.

This comprehensive and methodical approach not only highlights the catalytic potential of transition metal nanoclusters but also uncovers the underexplored promise of p-block metal nanoclusters, bridging the gap between conventional and unconventional materials. By identifying periodic trends and offering design principles for nanocluster-based catalysts, this work lays the groundwork for sustainable and efficient ammonia production technologies.

Furthermore, this study extends beyond traditional computational screening by offering experimentally relevant insights into the feasibility of nanocluster-based NRR catalysts. While small nanoclusters are often considered metastable, their stability can be significantly influenced by the choice of ligands, supports, or reaction conditions, which can enhance their practical viability. By systematically evaluating adsorption trends and potential-determining steps across a diverse range of nanoclusters, this work provides a predictive framework that experimentalists can leverage to synthesize and test the most promising candidates. The identification of stable adsorption configurations, coupled with charge transfer analyses, helps pinpoint key factors that govern catalytic efficiency at the nanoscale. These findings not only refine our fundamental understanding of NRR catalysis but also facilitate the rational design of stable, size-selected nanoclusters for real-world electrochemical applications.

The stability of small metal nanoclusters is indeed a critical factor in determining their practical applicability in electrochemical catalysis. It is well established that most small-sized metal clusters, including 10-atom clusters, can exhibit metastability, often requiring inert environments for synthesis and preservation. However, size-selected small nanoclusters have been experimentally demonstrated to behave differently from their bulk or larger counterparts, showing distinct electronic structures, binding affinities, and catalytic behaviors. Such experimental studies validate the importance of investigating nanoclusters at this size scale, as they can exhibit unique catalytic properties that are otherwise absent in larger clusters or bulk materials.

The overall aim of our work is a comprehensive evaluation of different metal nanoclusters to establish systematic trends in NRR activity. By analyzing a diverse range of nanoclusters, including metals from the 3d, 4d, 5d, and p-blocks, this study offers valuable insights into the fundamental structure–activity relationships that govern catalytic performance at the nanoscale. While the absolute stability of pristine 10-atom clusters in realistic electrochemical environments remains an open question, our work serves as a crucial first step in identifying promising candidates that warrant further experimental validation. The trends derived from this study provide a fundamental understanding of how metal composition and nanocluster size influence NRR performance, facilitating the rational design of stable and efficient electrocatalysts. Thus, rather than being a limitation, our approach lays the groundwork for experimentalists to explore the most promising nanoclusters under realistic electrochemical conditions, potentially leading to novel strategies for stabilizing and utilizing these clusters in practical applications.

Methods

Structural characterization and global minimum search

Accurately determining the global minimum configurations of nanoclusters is a crucial step in modeling nanocatalysts, as the catalytic activity and selectivity of these materials are often highly dependent on the size and shape of the nanoclusters. The potential energy surface (PES) for a given nanocluster composition is typically highly complex, with many possible geometrical arrangements that have very similar energies. This complexity is particularly pronounced for atomically precise, smaller-sized nanoclusters, where quantum size effects dominate, making an accurate description of the PES at the DFT level essential.

To locate the global minimum configurations of first-row transition metal (TM) nanoclusters, we employed the GIGA version of the Birmingham Parallel Genetic Algorithm (BPGA)[63–65] at the DFT level. The GA process begins by generating a set of random geometries—in this study, 10 initial geometries—which are then relaxed into local minima to form the initial population in the pool. Based on predefined crossover and mutation rates, the GA applies crossover and mutation operations to members of the pool to generate new structures. For the crossover operation, pairs of clusters are selected using a weighted roulette-wheel[66] selection method, and mating is

performed using a variant of the Deaven and Ho phenotypic cut-and-splice method,[67] resulting in a single offspring.

Various mutation operations, such as "move," "rotate," "twist," "partial inversion," and "rattle," are applied to randomly selected clusters *via* roulette-wheel selection. For instance, in skin mutation, 80% of the cluster atoms remain intact while 20% are repositioned randomly around the cluster. In rattle mutation, 40% of the atoms nearest to a randomly chosen atom are moved. Change core mutation alters the core of the cluster, while rotation and twist mutations rotate or twist a percentage of cluster atoms. Partial inversion operation inverts a subset of cluster atoms relative to their geometric center, and tunnel operation relocates the atom farthest from the center to the opposite side of the cluster. The objective of these operations is to maintain diversity within the pool, preventing stagnation after several generations.

We ran the genetic algorithm for a minimum of 400 generations, and in some cases, more than 1500 generations were required. Each generation involved the relaxation of newly generated geometries through crossover or mutation operations. To ensure the robustness of our results, we performed a parallel run for each cluster to confirm that both BPGA runs converged on the same global minimum configuration.

Locating global minimum configurations for adsorbate-bound nanoclusters

To accurately determine the most energetically preferred binding sites for adsorbates on the reoptimized global minimum configurations, we conducted an extensive search considering all possible unsymmetrical edges, metal atom sites, and various binding modes and orientations of the adsorbates. In addition to the global minimum configurations, we also included ten lower-energy configurations in our analysis, as the energy difference between the global minimum and these low-lying configurations is often minimal. This approach significantly increased the number of initial configurations considered for adsorbate binding and subsequent geometry relaxation. By performing such an extensive search on the cluster-adsorbate complexes, we ensured that the most stable adsorbate binding site on the nanocluster was accurately identified.

Density functional theory and relaxation protocol

For the determination of the global minimum configurations for both pure nanoclusters and adsorbate-bound nanoclusters, as well as the exploration of other low-energy structures, we employed spin-polarized density functional theory (DFT) calculations using the Vienna ab initio simulation package (VASP).[68–71] The Perdew–Burke–Ernzerhof (PBE)[72] exchange–correlation functional within the generalized gradient approximation (GGA) framework was used, along with projected augmented wave (PAW)[73] pseudopotentials to describe ion–electron interactions. An initial plane wave cutoff energy of 400 eV was used, and Methfessel-Paxton[74] smearing with a sigma value of 0.01 eV was applied to enhance convergence. Following identification of the global minimum, the geometries were re-optimized with a more stringent convergence criterion (10^{-6} eV for energy and 0.01 eV Å^{-1} for force) and a higher plane wave cutoff energy of 600 eV to ensure accurate geometries and energy values. van der Waals interactions were included through Grimme's DFT-D3[75,76] method during the re-optimization process.

The most stable adsorbate configurations on each nanocluster were determined by optimizing the cluster-adsorbate complexes using the same DFT protocol (PBE functional, DFT-D3 corrections, and higher plane wave cutoff energy). The Bader[77] method was employed for charge analysis on these optimized structures. The free energies of the adsorbates were calculated by performing vibrational analysis, assuming the nanoclusters were immobilized on supports. Thermal corrections, including zero-point energy, enthalpy, and entropy corrections, were computed using harmonic vibrational frequencies at 298.15 K with VASPKIT.[78] These corrections were added to the DFT electronic energies to obtain the Gibbs free energies of the adsorbates, which are reported as standard values (ΔG^0) calculated at 298.15 K.

Computational hydrogen electrode model

The computational hydrogen electrode (CHE)[79,80] model was applied to calculate the reaction free energy changes (ΔG) for various electrochemical steps. In this model, the free energy change for an electrochemical step is given by:

$$\Delta G[A^* + (H^+ + e^-) \rightarrow AH^*] = \mu(AH^*) - \mu(A^*) - [\mu(H^+) + \mu(e^-)]$$

The chemical potential of the proton–electron pair (H^+/e^-) is equivalent to half the chemical potential of the gas-phase H_2 molecule:

$$(H^+) + \mu(e^-) = 0.5\mu(H_2(g)) - |e|U$$

At an applied potential U, the free energy of the proton–electron pair shifts by $-|e|U$, making the NRR step less endergonic at negative applied potential biases. The limiting potential (UL) is defined as the minimum applied bias that renders all electrochemical steps exergonic (downhill) in free energy. Under standard conditions, the free energy change is given by:

$$\Delta G = \Delta G^0 + |e|U$$

For the reaction to be spontaneous, ΔG must be less than or equal to zero. The rate limiting potential (RLP) corresponds to the highest endergonic step in the reaction pathway and is always negative, measured in volts (V), while the corresponding free energy of the potential-determining step (PDS) is positive, measured in electron volts (eV).

Previous studies have shown that hydrogen bond stabilization introduces a small correction, approximately 0.08 eV per bond.[54,81] Consequently, the overall impact on the onset potentials in our calculations is expected to be minimal, with changes likely to be less than 0.1 eV.[54,81] Given the negligible effect, and consistent with previous studies, we have chosen not to include these corrections, as they would not significantly influence our results.

Results and discussions

Geometries of global minimum of nanoclusters and adsorbate-bound nanoclusters

The global minimum configurations of all nanoclusters, as well as the most stable binding sites of all adsorbates on these nanoclusters, were determined as described in the Methods section. We observed that the adsorption of species on nanocluster surfaces often induces significant geometrical rearrangements in the nanoclusters, deviating from their global minimum configurations to achieve a more stable adsorbate-bound geometry. These geometric rearrangements require energy, and this factor should be considered when discussing adsorption free energies or the free energies associated with electrochemical steps as the adsorption energies are calculated based on these new geometries relative to the global minimum configuration. Such geometric rearrangements are rarely seen on bulk metal and metal oxide surfaces or in larger nanoparticles, where the surface structure tends to remain relatively unchanged upon adsorption. This highlights a key distinction between electrocatalytic processes on metal surfaces and those occurring on metal nanoclusters, underscoring the need to treat these systems separately when evaluating catalytic performance.

Fig. 1 illustrates the global minimum configurations of the nanoclusters, along with selected examples of adsorbate-bound structures. Additionally, Tables S1 and S2 (ESI†) provides detailed bond distances for N–metal and N–N, across all adsorbates. Notably, the N–N bond distance is significantly elongated on early transition metal nanoclusters, ranging from approximately 1.33 Å to 1.35 Å. This elongation serves as a strong indicator of N_2 activation on these early TMs, reflecting their high propensity for facilitating the initial nitrogen bond cleavage. Similarly, mid-transition metal nanoclusters, including Ta, Nb, V, W, Tc, Cr, and Mn, exhibit moderate N_2 activation, as evidenced by their elongated bond distances in the range of 1.31 Å to 1.20 Å.

In contrast, late transition metal nanoclusters such as Cu, Ag, and Au do not exhibit significant elongation in N–N bond distances. Similar trends are observed for p-block and pseudo-p block metal nanoclusters, suggesting minimal activation of N_2 on these metal surfaces. This minimal elongation is indicative of a lower catalytic efficiency for N_2 activation on these metal nanoclusters. The distinct variation in N–N bond elongation across different metal categories underscores the varying degrees of N_2 activation, which correlates with the electronic properties of the metals studied.

In our previous work on CO_2 reduction using first-row transition metal (TM) nanoclusters, we identified 3 to 10 global minimum (GM) configurations for Sc–Cu nanoclusters.[82] Additionally, we conducted a detailed comparison of the GM structures and low-lying geometric configurations obtained

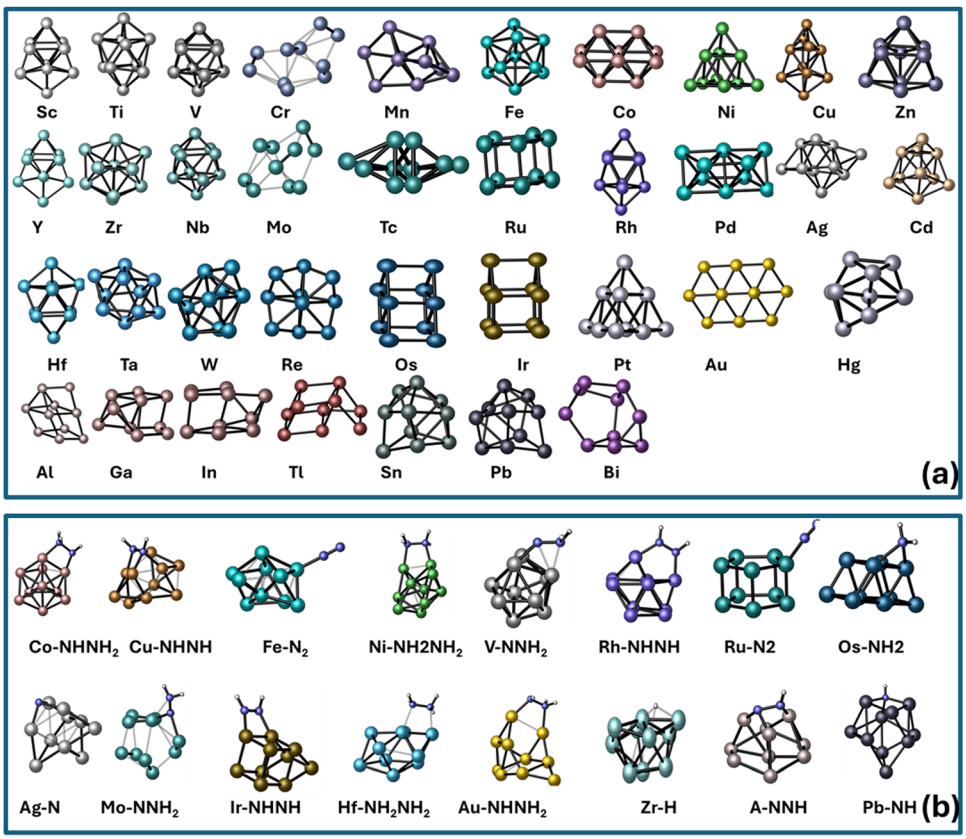

Fig. 1 (a) Global minimum (GM) configurations of 10-atom nanoclusters used in the study, comprising 3d, 4d, and 5d transition metals as well as p-block metals; (b) selected adsorbate-bound nanocluster complexes.

from the Basin-Hopping Particle Swarm Genetic Algorithm (BPGA) method with those reported in the literature.[83–104] In Our analysis revealed that different computational methods and variations in DFT settings can sometimes lead to different GM configurations due to differences in convergence criteria and energy landscapes. However, despite these variations, all studies consistently identified the same set of geometric configurations within the low-energy nanocluster regime. While the relative energetic ordering of these configurations may change across different methods, the low-lying isomers remain energetically competitive and are likely to coexist under realistic conditions.

Given the close energetic proximity of these low-energy isomers, we extended our analysis beyond the global minimum configurations to ensure a comprehensive evaluation of adsorbate binding. To ensure a thorough assessment of adsorbate binding on nanoclusters, we extended our analysis beyond the global minimum configurations by incorporating ten low-energy isomers, as their energy differences from the global minimum were often minimal. Given the competitive stability of these low-lying isomers, we conducted an extensive search to determine the most energetically favorable binding sites. This involved exploring all possible unsymmetrical edges, metal atom sites, and diverse binding modes and orientations of the adsorbates. By systematically evaluating cluster-adsorbate interactions across a wider range of configurations, we enhanced the accuracy of identifying the most stable adsorbate binding sites. This approach provides a more comprehensive understanding of the active sites that influence catalytic performance, ensuring that structural variations among low-energy isomers are accounted for in our analysis.

N_2 adsorption

Fig. 2(a) presents the adsorption free energies of N_2 on a diverse range of metal nanoclusters, revealing distinct trends across the 3d, 4d, and 5d transition metal series, as well as p-block metals. Within the 3d transition metals, scandium (Sc) and titanium (Ti) demonstrate notably strong interactions with N_2, exhibiting adsorption free energies of −3.88 eV and −3.43 eV, respectively. Scandium, in particular, shows the most negative adsorption free energy, indicating its superior efficacy for N_2 adsorption among the all metals. Other 3d metals such as vanadium (V), chromium (Cr), manganese (Mn), and nickel (Ni) show moderately negative adsorption free energies, ranging from −0.70 eV to −0.47 eV, suggesting reasonable affinity for N_2. In contrast, iron (Fe), cobalt (Co), and copper (Cu) nanoclusters exhibit less negative to slightly positive adsorption free energies, indicating weaker interactions with N_2. Zinc (Zn), although part of the 3d series, displays a slightly positive adsorption energy, aligning more closely with the adsorption behaviour observed in p-block metals, indicating less favourable adsorption characteristics.

In the 4d block, yttrium (Y) and zirconium (Zr) stand out with strong negative adsorption free energies of −3.49 eV and −3.44 eV, respectively. The adsorption energies of other 4d transition metal nanoclusters vary from weak to moderate, with technetium (Tc), ruthenium (Ru), rhodium (Rh), and palladium (Pd) exhibiting moderate adsorption free energies ranging from −0.83 eV to −0.59 eV. Niobium (Nb) and molybdenum (Mo) show mildly favorable adsorption energies of −0.29 eV and −0.13 eV, respectively. In contrast, silver (Ag) and cadmium (Cd) exhibit positive adsorption free energies, indicating weaker interactions with N_2. Cadmium, despite being a 4d metal, mirrors the p-block behaviour seen in zinc, with a positive adsorption energy that suggests less effective N_2 adsorption.

Among the 5d transition metals, hafnium (Hf) exhibits the most negative adsorption free energy at −3.54 eV, indicating a highly favorable interaction with N_2. Tungsten (W) also shows strong adsorption, with a free energy of −1.37 eV, the most negative among the mid-transition metals in the 5d series. Other 5d metals, including rhenium (Re), osmium (Os), tantalum (Ta), iridium (Ir), and platinum (Pt), display moderate adsorption free energies in the range of −0.86 eV to −0.32 eV. Gold (Au) and mercury (Hg), however, exhibit slightly positive adsorption energies, indicating weaker adsorption characteristics. It is noteworthy that lanthanum (La), a 5d metal, was not included in this analysis.

The p-block metal nanoclusters, including aluminum (Al), gallium (Ga), indium (In), thallium (Tl), tin (Sn), lead (Pb), and bismuth (Bi), predominantly exhibit positive adsorption free energies for N_2, reflecting very weak or unfavorable adsorption. This trend underscores the lesser suitability of these metals for N_2 adsorption applications compared to transition metals, which generally exhibit negative adsorption free energies.

Overall, the analysis reveals that early transition metal nanoclusters, particularly those with d^1 and d^2 electronic configurations, exhibit significantly larger negative adsorption free energies, indicating strong N_2 adsorption potential. In contrast, mid- and late-transition metal nanoclusters show weaker to moderate N_2 adsorption characteristics. Metals with a completely filled d-shell configuration (d^{10}), such as Zn, Cd, and Hg, do not exhibit favorable adsorption free energies, as evidenced by their positive values. These metals, although traditionally considered transition metals, exhibit adsorption behaviors more akin to p-block metals and are therefore classified as ''pseudo-p-block'' metals in this context. This analysis highlights the critical role of electronic configuration and metal selection in optimizing N_2 adsorption or activation for catalytic applications.

Here after to make our studies across various d and p-block metal nanoclusters, we use the following classifications:

(a) Early transition metals: TM with d^1 and d^2 configurations (Sc, Ti, Y, Zr, Hf)

(b) Mid transition metals: TM with d^3 to d^7 configurations (V, Cr, Mn, Fe, Co, Nb, Mo, Tc, Ru, Rh, Ta, W, Re, Os, and Ir)

(c) Late transition metals: TM with d^8 to d^9 configurations (Ni, Cu, Pd, Ag, Pt and Au)

(d) Pseudo P-block metals: d^{10} configurations (Zn, Cd, and Hg)

(e) P-Block metals. (Al, Ga, In, Tl, Sn, Pb, and Bi)

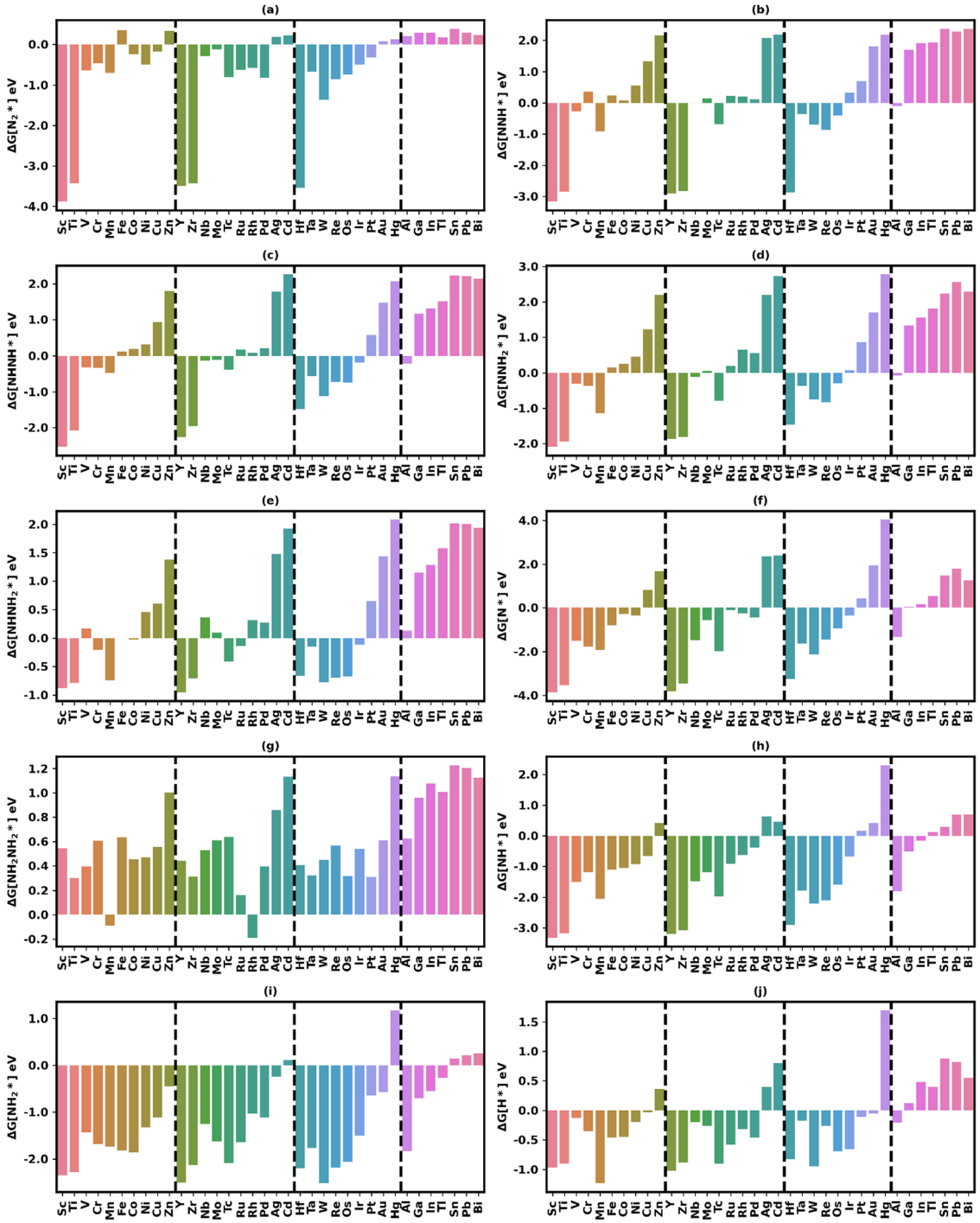

Fig. 2 Adsorption free energies (ΔG; eV) of key NRR intermediates, including (a) N_2*, (b) NNH*, (c), NHNH*, (d) NNH_2*, (e) $NHNH_2$*, (f) N*, (g) NH_2NH_2* (h) NH, (i) NH_2* and (j) H*on various metal nanoclusters. The panels highlight distinct trends in adsorption free energies across early, mid, and late transition metals, as well as p-block and pseudo-p block metals.

Electrochemical reduction of N_2 (NRR)

In this study, we exclusively focused on the associative mechanism for the nitrogen reduction reaction (NRR), as it is more suitable for the ambient conditions typically used in electrochemical catalysis. The dissociative mechanism, which involves the cleavage of the N_2 triple bond prior to hydrogenation, is associated with industrial processes like the Haber–Bosch method due to its requirement for high pressure and temperature. The direct cleavage of the N≡N bond requires a substantial energy input (ΔH = 941 kJ mol^{-1}),[10] making this pathway highly energy-intensive and impractical for electrochemical reduction, which typically occurs under atmospheric pressure and room temperature conditions.

In contrast, the associative mechanism is more favorable under mild electrochemical nitrogen reduction reaction (NRR) conditions, as it bypasses the need for N≡N bond dissociation, thereby avoiding the high energy demand associated with N_2 bond cleavage. The reaction proceeds *via* six proton-coupled electron transfer (PCET) steps, making it particularly feasible for electrochemical systems. Given these conditions, we excluded both the dissociative mechanism and the enzymatic pathway, which typically involves the side-on binding of N_2, as seen in biological nitrogenases or extended metal surfaces. Nanoclusters, with their limited surface area and distinct structural properties, do not accommodate such configurations. Instead, we meticulously explored every potential binding site and orientation for N_2 on nanoclusters, ensuring we captured the most stable arrangement that supports the associative mechanism.

The associative mechanism is further categorized into:

- Associative alternating pathway: hydrogenation occurs alternately on both nitrogen atoms, resulting in the sequential release of two ammonia molecules.
- Associative distal pathway: hydrogenation occurs primarily on one nitrogen atom before the second, leading to the sequential release of two ammonia molecules.

The NRR associative pathways involve key intermediates such as *NNH, *NHNH, *NNH_2, *$NHNH_2$, *NH_2NH_2, *N, *NH, and *NH_2. The following section provides a detailed analysis of the energetics associated with each PCET step across these intermediates.

Our study focuses predominantly on the associative mechanism, encompassing both the distal and alternating pathways. In addition, we explore mixed-type pathways, including the distal-alternating (I) and (II) pathways, as well as the alternating-distal (I) pathway. These mixed-type pathways, which are typically underexplored in previous studies of NRR over heterogeneous catalysts, offer novel insights into the NRR mechanism.

$$\text{Path I: } * + N_2 \rightarrow NNH^* \rightarrow NNH_2^* \rightarrow N^* \rightarrow NH^* \rightarrow NH_2^* \rightarrow * \quad \text{Distal}$$

$$\text{Path II: } * + N_2 \rightarrow NNH^* \rightarrow NNH_2^* \rightarrow NHNH_2^* \rightarrow NH^* \rightarrow NH_2^* \rightarrow * \quad \text{Distal-alternative mixed I}$$

$$\text{Path III: } * + N_2 \rightarrow NNH^* \rightarrow NNH_2^* \rightarrow NHNH_2^* \rightarrow NH_2NH_2^* \rightarrow NH_2^* \rightarrow * \quad \text{Distal-alternative mixed II}$$

$$\text{Path IV: } * + N_2 \rightarrow NNH^* \rightarrow NHNH^* \rightarrow NHNH_2^* \rightarrow NH^* \rightarrow NH_2^* \rightarrow * \quad \text{Alternative-distal mixed (I)}$$

$$\text{Path V: } * + N_2 \rightarrow NNH^* \rightarrow NHNH^* \rightarrow NHNH_2^* \rightarrow NH_2NH_2^* \rightarrow NH_2^* \rightarrow * \quad \text{Alternative}$$

In the distal-alternative (I) and (II) mixed-type pathways, the reaction initially proceeds through the distal mechanism up to the formation of the NNH_2* intermediate. Following this, the reaction forms the $NHNH_2$* species *via* the alternative mechanism by hydrogenating the non-terminal nitrogen atom. In contrast, the alternative-distal mixed (I) mechanism begins with the alternative pathway, leading to the formation of the $NHNH_2$* species, after which it transitions to the distal mechanism, resulting in the formation of NH* species.

In this study, we have not explicitly considered the enzymatic mechanism for NRR. While both the associative alternative and enzymatic mechanisms follow the same stepwise hydrogenation pathway, they primarily differ in how N_2 binds to the catalyst. The associative alternative mechanism typically involves end-on binding, whereas the enzymatic mechanism features side-on binding on well-defined active sites. However, due to the structural diversity of nanoclusters and the absence of a uniform metal arrangement as in metal or metal oxide surfaces, it is challenging to distinctly classify N_2 adsorption as strictly end-on or side-on.

By systematically exploring adsorption at metal–metal edges and metal binding sites, we identified the most favorable binding configurations without imposing a predefined mechanistic constraint. Our study considered all possible adsorption configurations for N_2 on nanoclusters, including both end-on and side-on orientations. Since both mechanisms share similar reduction steps, the enzymatic mechanism was not explicitly examined but was inherently included in our analysis. However, our approach inherently captures all possible binding orientations relevant to nanocluster catalysis.

First electrochemical proton–electron transfer step. The first electrochemical step in the nitrogen reduction reaction (NRR) involves the hydrogenation of the N_2 to form the NNH* intermediate. This process is facilitated by the transfer of a proton–electron pair ($H^+ + e^-$) to N_2. Fig. 2(b) illustrates the adsorption free energies of the NNH* intermediate on various metal nanoclusters, revealing trends that align closely with those observed for N_2* adsorption.

Our findings indicate that nanoclusters composed of early transition metals from the 3d, 4d, and 5d series—specifically scandium (Sc), titanium (Ti), yttrium (Y), zirconium (Zr), and hafnium (Hf)—exhibit significantly more favorable adsorption free energies for NNH*, typically around −3.0 eV. This suggests that these nanoclusters form stable, exergonic NNH* adsorbates on their surfaces. Conversely, nanoclusters made from mid to late transition metals tend to show weaker adsorption affinities, as evidenced by relatively lower or even positive adsorption free energies.

Among the mid to late transition metals, only a select few—namely vanadium (V) and manganese (Mn) from the 3d series, technetium (Tc) from the 4d series, and tantalum (Ta), tungsten (W), rhenium (Re), and osmium (Os) from the 5d series—exhibit modest but favourable negative adsorption free energies ranging from −0.9 eV to −0.3 eV. Notably, late transition metals such as copper (Cu), gold (Au), and silver (Ag) display significantly positive adsorption free energies, indicating a much weaker propensity for NNH* adsorption.

Additionally, nanoclusters composed of p-block metals with the exception of aluminium (Al) and pseudo p-block metals, namely zinc (Zn), cadmium (Cd), and mercury (Hg), exhibit

significantly larger positive adsorption free energies for NNH* (>1.7 eV), indicating their limited effectiveness in facilitating NNH* formation during the nitrogen reduction reaction (NRR). In contrast, aluminium (Al) does not conform to this trend, displaying a small negative free energy (−0.10 eV), suggesting a slight advantage in promoting NNH* formation compared to its p-block counterparts.

Interestingly, the adsorption free energies for NNH* are consistently lower than those for N_2* adsorption across the nanoclusters studied. Fig. 3(a) highlights the differences in adsorption free energies between N_2* and NNH*, serving as an indicator of the relative stabilities of these intermediates on nanocluster surfaces. For instance, the adsorption free energies for N_2* on Sc and Ti are −3.88 eV and −3.43 eV, respectively, which decrease to −3.16 eV and −2.85 eV for NNH*. Only three metal nanoclusters—manganese (Mn), iron (Fe), and aluminum (Al)—exhibit a higher preference for NNH* adsorption compared to N_2* adsorption. These observations suggest that early transition metal nanoclusters, particularly those of Sc, Ti, Y, Zr, and Hf, may serve as promising catalysts for N_2 activation and subsequent NNH* formation.

Second electrochemical proton–electron transfer step. In the subsequent electrochemical step of the nitrogen reduction reaction (NRR), the NNH* species can evolve into either NHNH* or NNH_2* intermediates. The adsorption free energies for these intermediates, as shown in Fig. 2(c) and (d), exhibit a consistent trend across different metal nanoclusters. Early transition metals generally display larger adsorption energies (>1.45 eV) for both adsorbates, while moderate to weak or even positive adsorption free energies are observed as one moves across the periodic table.

Among the mid-transition metals, several nanoclusters from the 5d series—specifically tantalum (Ta), tungsten (W), rhenium (Re), and osmium (Os), and tantalum (Ta) —exhibit favorable negative adsorption free energies for NHNH*, ranging from −1.12 eV to −0.56 eV. Additionally, nanoclusters composed of vanadium (V), chromium (Cr), and manganese (Mn) from the 3d transition metal block; and technetium (Tc) from the 4d transition metal block; and aluminium (Al) from the p-block also demonstrate favorable adsorption free energies for NHNH*, with values between −0.47 eV and −0.21 eV.

For NNH_2* adsorption, a similar pattern is observed with minor variations. Nanoclusters of V, Cr, and Mn from the 3d block; Nb, and Tc from the 4d block; and Ta, W, Re, and Os from the 5d block, as well as Al from the p-block, exhibit negative adsorption free energies. Notably, Mn, Re, Tc and W show strong adsorption free energy values ranging from −1.14 eV to −0.74 eV, while all other metal nanoclusters display adsorption free energies above −0.36 eV. We have observed that, with the single exception of aluminum, all other p-block and pseudo p-block metals display large positive adsorption free energies for both NHNH* and NNH_2* adsorbates.

The feasibility of forming intermediates during the NRR critically depends on the free energy changes associated with each electrochemical step. Fig. 4 presents the free energy changes for the formation of NNH_2* and NHNH* from NNH*, where negative values denote exergonic (thermodynamically favorable) processes and positive values denote endergonic (thermodynamically unfavorable) processes.

Early TMs exhibit significantly larger endergonic free energy changes for the electrochemical step NNH* → NHNH*, attributed to the strong stabilization of the NNH* intermediate,

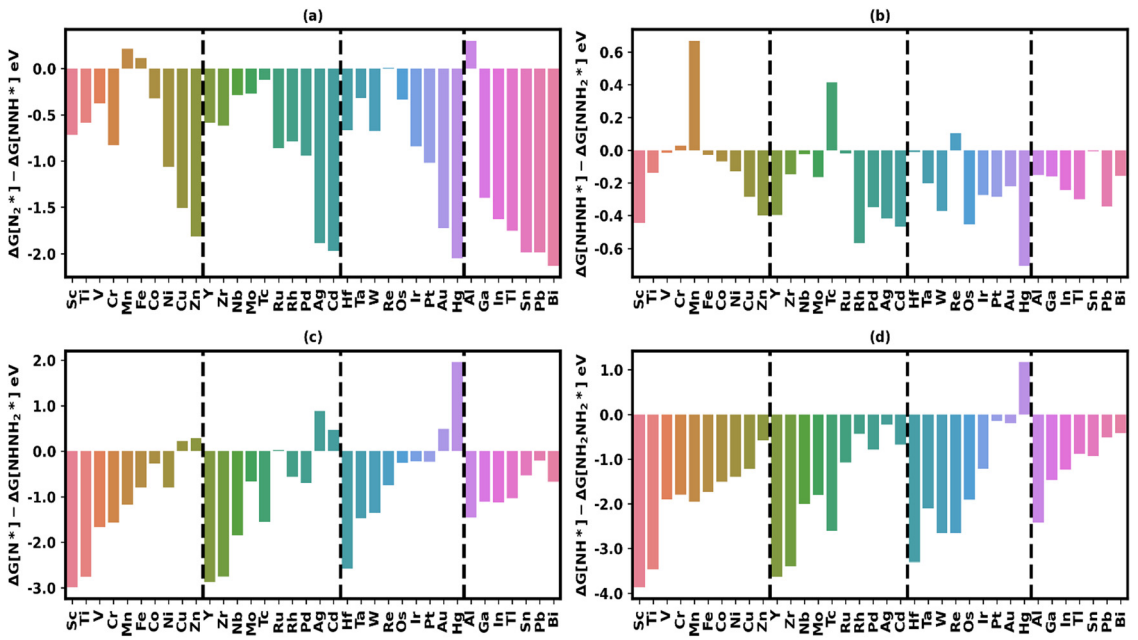

Fig. 3 Relative stabilities of various adsorbate pairs (a–d), determined by the difference in their adsorption free energies, ΔG(A*) − ΔG(B*) in eV, indicating the relative preference between adsorbates A* and B*. If the difference in free energy is negative, A* is more stable than B*; conversely, if the difference is positive, B* is more stable than A*.

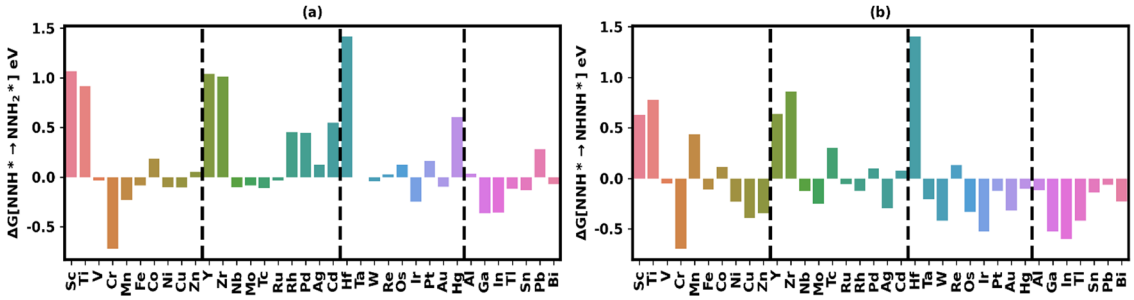

Fig. 4 Free energy changes (ΔG, eV) associated with the second proton-coupled electron transfer (PCET) step in the electrochemical nitrogen reduction reaction (NRR). Panels (a) NNH* → NNH_2* and (b) NNH* → NHNH*.

which impedes further conversion to NHNH*. In contrast, several metal nanoclusters from mid- and late-TMs, as well as p-block and pseudo-p-block metals, display favorable exergonic free energy changes, with moderate values ranging from −0.7 eV to −0.3 eV. Additionally, other metal nanoclusters exhibit relatively small exergonic to mildly endergonic free energy changes (−0.3 eV to +0.13 eV), indicating a near-thermoneutral to slightly unfavorable process.

For the NNH* → NNH_2* step, only a limited number of metal nanoclusters—specifically those of Cr, Ga, In, Ir, and Mn—show favorable exergonic free energy changes, ranging from −0.75 eV to −0.23 eV. In contrast, most other metal nanoclusters, excluding early transition metals, exhibit mild exergonic to moderate endergonic free energy changes for this step, indicating a less favorable or unfavorable thermodynamic process. Early transition metals once again stand out, with significantly larger endergonic free energy changes, further emphasizing the difficulty of forming the NNH_2* intermediate on these surfaces from NNH*.

To elucidate this preference for the formation of NHNH* or NNH_2* from NNH*, we plotted the relative stability of the two intermediates, NNH_2* and NHNH*, on the nanoclusters by calculating the difference in their adsorption free energies. The analysis, depicted in Fig. 3(b), indicates an overall preference for the formation of NHNH* over NNH_2* on most nanoclusters. However, the relatively small differences in preference values (less than 0.2 eV) for most metal nanoclusters suggest that both intermediates are feasible to form at relatively low potentials. Interestingly, Mn and Tc, are the only metal nanoclusters that show a greater preference for the formation of NNH_2* over NHNH* and Re exhibit mild preference.

Overall, these observed trends emphasize the critical role of metal selection in optimizing the NRR pathway, particularly in the context of stabilizing or destabilizing key intermediates such as NNH*, NHNH*, and NNH_2*. The findings highlight the challenges associated with early transition metals in progressing beyond the NNH* intermediate due to the high energy barriers linked with the formation of subsequent intermediates. The exergonicity observed for p-block and pseudo-p-block metals primarily arises from the transition between two endergonic states, where the final state has a relatively lower energy.

Third electrochemical proton–electron transfer step. In the third electrochemical step of the nitrogen reduction reaction (NRR), $NHNH_2$* can form either from NHNH* by hydrogenating the terminal nitrogen atom or from NNH_2* by hydrogenating the non-terminal nitrogen atom. Alternatively, N* can be formed from NNH_2* by eliminating NH_3. The adsorption free energies for $NHNH_2$* and N* are depicted in Fig. 2(e) and (f).

Aside from early transition metal nanoclusters, only a few exhibit favorable negative adsorption free energies for $NHNH_2$*. These include chromium (Cr) and manganese (Mn) from the 3d block, technetium (Tc) and ruthenium (Ru) from the 4d block, and tantalum (Ta), tungsten (W), rhenium (Re), osmium (Os), and iridium (Ir) from the 5d block. Among these, Mn, Tc, W, Re, and Os show favorable adsorption free energy values ranging from −0.78 eV to −0.41 eV. All p-block metal nanoclusters, with the exception of aluminum, exhibit significantly larger unfavorable positive adsorption free energies, ranging from 1.15 eV to 2.0 eV. In contrast, aluminum shows a much smaller positive adsorption free energy of 0.13 eV.

In general, the adsorption free energies for N* are significantly more negative for most d-block metal nanoclusters, with the exception of late transition metals (TMs). All p-block metals, except aluminum (Al), along with pseudo p-block metals and late TMs such as Cu, Ag, Pt, and Au, exhibit unfavorable positive adsorption energies for N*. Notably, the adsorption free energies for N* intermediates are similar to those observed for N_2*. Mid-transition metals display more negative adsorption free energies for N*, ranging from −2.1 eV to −0.3 eV across the 3d, 4d, and 5d blocks. Specifically, W, Tc, Mn, Cr, Ta, V and Nb show values between −2.1 eV and −1.5 eV, while Re, Al, and Os have values between −1.50 eV and −0.90 eV. Furthermore, adsorption free energies tend to decrease across the periodic table, especially after the d^5 configuration, where they become positive or nearly zero. Among the p-block metals, aluminum is notable for its favorable adsorption energy of −1.33 eV for N*.

The relative stabilities of $NHNH_2$* and N*, determined from the difference in their adsorption free energies as shown in Fig. 3(c), demonstrate a clear thermodynamic preference for N* over $NHNH_2$*. This implies that when there is competition between the formation of $NHNH_2$* and N* from a common precursor such as NNH_2*, N* is preferentially formed. Interestingly, a few metal nanoclusters, including Cu, Zn, Ag, Cd, Au, and Hg, exhibit greater stabilization for $NHNH_2$* compared to

N*, although both intermediates display unfavorable positive adsorption free energies.

The electrochemical step favoring the formation of N* from NNH_2* (as shown in Fig. 5a) is strongly exergonic across most nanoclusters, with the notable exceptions of Ag, Au, and Hg. The exergonicity of these free energy changes generally decreases as one progresses from early to mid to late transition metals. In contrast, the formation of $NHNH_2$* from NNH_2* or NHNH* (Fig. 5c and e) is typically endergonic or only mildly exergonic on most d-block nanoclusters.

For the NNH_2* → $NHNH_2$* step, only a limited number of metal nanoclusters exhibit favorable exergonic free energy changes. Excluding early TMs, which show significantly larger endergonic free energy changes for this step, mid- and late transition metals such as Ag, Cu, Os, Rh, Ru, Co, Pd, Au, Pt, and Ir display favorable exergonic free energy changes, ranging from −0.7 eV to −0.2 eV. Additionally, p-block and pseudo-p-block metal nanoclusters also demonstrate favorable exergonic free energy changes. A similar trend is observed for the electrochemical step NHNH* → $NHNH_2$*, where the process is predominantly endergonic on most nanoclusters. However, favorable exergonic free energy changes occur on select nanoclusters, particularly mid- and late transition metals such as Cu, Ru, Ag, Mn, and Co, with values ranging from −0.3 eV to −0.2 eV. P-Block and pseudo p-block metals also exhibit favorable adsorption free energies. Furthermore, the NHNH* → $NHNH_2$* step is generally more endergonic compared to NNH_2* → $NHNH_2$*, correlating with the higher thermodynamic stability of NHNH* relative to NNH_2*, as previously discussed. A general trend from unfavorable endergonic free energy changes to favorable exergonic free energy changes is observed as one moves from early to late transition metals for these two electrochemical steps.

Moreover, late transition metals, as well as p-block and pseudo p-block metals, exhibit exergonic free energy changes for the electrochemical step leading to the formation of $NHNH_2$* from either NNH_2* or NHNH*. However, caution is warranted, as these cases represent a transition from a more endergonic to a less endergonic thermodynamic state. For instance, the adsorption free energy of NNH_2* on a Pb nanocluster is 2.56 eV, while that for $NHNH_2$* is 2.00 eV, indicating an exergonic step with the release of 0.56 eV.

It is crucial to recognize that the feasibility of forming N* intermediates is highly dependent on the preceding reaction pathways, particularly whether NNH_2* or NHNH* is formed from NNH* in the second electrochemical step. If NNH_2* is formed, it leads exclusively to the formation of N* through a highly exergonic step on all nanoclusters. Conversely,

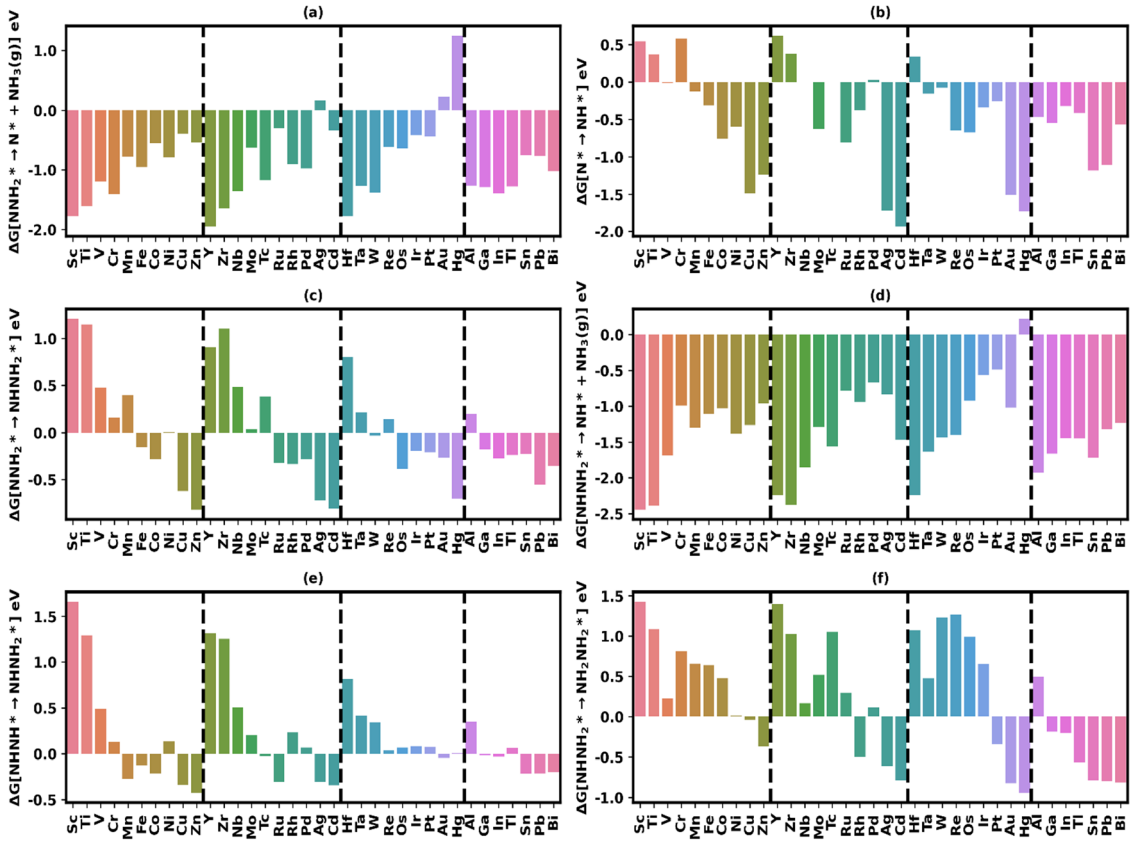

Fig. 5 Free energy changes (Δ*G*, eV) for the third (left) and fourth (right) electrochemical steps in the nitrogen reduction reaction (NRR). The third steps include (a) NNH_2* → N*, (c) NNH_2* → $NHNH_2$*, and (e) NHNH* → $NHNH_2$*. The fourth steps include (b) N* → NH*, (d) $NHNH_2$* → NH*, and (f) $NHNH_2$* → NH_2NH_2*.

if NHNH* is formed in the second electrochemical step, the third electrochemical step must overcome more endergonic free energy changes to form $NHNH_2$*.

Fourth electrochemical proton–electron transfer step. In the fourth electrochemical step, three possible pathways emerge: NH* can form from either N* or $NHNH_2$*, and NH_2NH_2* can form from $NHNH_2$*. The NH* species exhibit significant stabilization on most nanocluster metal surfaces, similar to N* (see Fig. 2(h)). As previously observed, early transition metals (TMs) show significantly larger negative adsorption free energies, with values becoming less negative as one moves across the periodic table from early to late TMs. Notably, the p-block metals Al, Ga, and In display favorable negative adsorption free energies of −1.80 eV, −0.51 eV, and −0.16 eV, respectively.

In contrast, NH_2NH_2* generally exhibits unfavorable positive adsorption free energy values on all nanoclusters as shown in Fig. 2(g), with the exceptions of Mn and Rh, which show small favorable adsorption free energies of −0.10 eV and −0.19 eV, respectively. This suggests that the hydrogenation of $NHNH_2$* on the non-terminal nitrogen atom is a highly disfavored electrochemical step. Consequently, if $NHNH_2$* is formed in the third electrochemical step, it predominantly leads to the formation of NH* on most nanoclusters. The relative preference for NH* over NH_2NH_2* is clearly illustrated in Fig. 3(d), which depicts the relative stability of these two intermediates on most nanoclusters, calculated from the difference in their free energy values.

Fig. 5(b), (d) and (f) present the free energy changes associated with the three electrochemical steps: N* → NH*, $NHNH_2$* → NH*, and $NHNH_2$* → NH_2NH_2*. The N* → NH* step is generally exergonic on most nanoclusters, with a few exceptions where moderate endergonic free energies are observed, particularly among early TMs. Typically, the free energy change for the N* → NH* transition shifts from endergonic in early TMs to mild to moderately large exergonic values in mid- and late TMs. Furthermore, this step is highly exergonic for p-block and pseudo p-block metals.

The electrochemical step $NHNH_2$* → NH* exhibits significantly large exergonic free energy changes across all nanoclusters, driven by the transition from the less stable $NHNH_2$* to the more thermodynamically stable NH* species. This step is highly exergonic for early transition metals (TMs) but decreases as one moves toward late TMs, with exergonic free energy changes ranging from −2.44 eV to −0.49 eV; the only exception is Hg, which shows a small endergonic free energy change of 0.23 eV.

Conversely, the $NHNH_2$* → NH_2NH_2* step is predominantly endergonic, with only a few exceptions among p-block and pseudo-p block metals, which exhibit unfavorable adsorption free energies for both $NHNH_2$* and NH_2NH_2*. Late transition metals such as Au, Ag, and Pt display relatively higher favorable exergonic free energy changes of −0.82 eV, −0.61 eV, and −0.34 eV, respectively, while the mid-transition metal Rh nanocluster shows a favorable exergonic free energy of −0.50 eV.

Fifth electrochemical proton–electron transfer step. In the fifth electrochemical step of the NRR, NH_2* is formed either from NH* or NH_2NH_2*, exhibiting significantly higher adsorption energy values, as shown in Fig. 2(i), which indicates a greater stabilization of this intermediate. Notably, p-block metals Al, Ga, In, and Tl exhibit favorable adsorption of NH_2* species, with Al showing a particularly favorable adsorption energy of −1.83 eV for NH_2*.

The transition from NH* to NH_2* (Fig. 6a) is generally characterized by favorable exergonic free energy changes except on early transition metal nanoclusters. Mid-transition metal nanocluster, with few exceptions, exhibit moderate exergonicity, while late transition metals display larger exergonic free energy changes for the NH* → NH_2* electrochemical step. The trend is evident, with early TMs showing higher endergonicity, and as one moves from early to late TMs, the free energy changes shift from endergonic to increasingly exergonic.

Conversely, the NH_2NH_2* → NH_2* step (Fig. 6b) is associated with significantly larger exergonic free energy changes, primarily due to the transformation of the highly endergonic NH_2NH_2* adsorbate into the highly stable NH_2* adsorbate on all nanoclusters. In this case, the trend is reversed, with early TMs exhibiting larger exergonic free energy changes, and the exergonicity decreasing as we move from early to late TMs. The exergonicity of this step falls within the range of −2.97 eV to −0.85 eV.

Sixth electrochemical proton–electron transfer step. In the sixth and final electrochemical step of the nitrogen reduction reaction (NRR), the nanocluster surface is regenerated by the removal of the adsorbed NH_2* species. For most nanoclusters, this regeneration step is significantly endergonic as shown in Fig. 7(a), particularly among early transition metals, which exhibit endergonicities ranging from 1.39 eV to 1.71 eV.

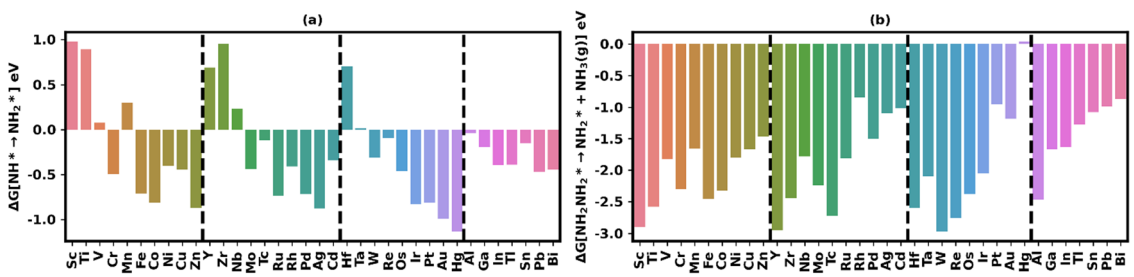

Fig. 6 Free energy changes (ΔG, eV) in the fifth electrochemical step (a) NH* → NH_2* and (b) NH_2NH_2* → NH_2*.

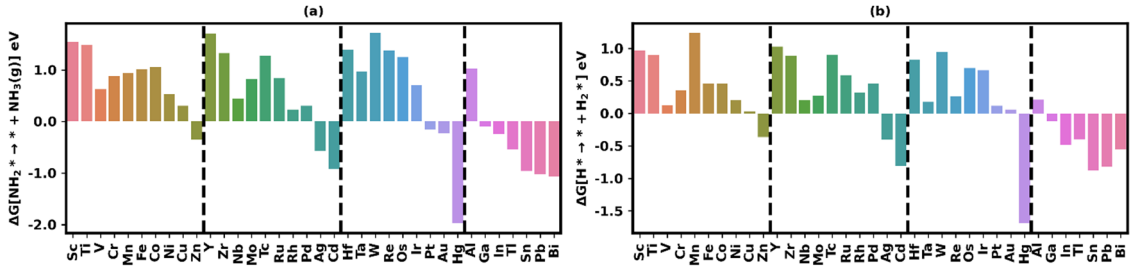

Fig. 7 Free energy changes (Δ*G*, eV) in the sixth and final electrochemical step (a) NH_2* → * + NH_3(g). Panel (b) shows the free energy changes for the desorption of adsorbed H* species.

Mid-transition metals show a spectrum of endergonic free energy changes between 1.71 eV and 0.3 eV. Several transition metals, including Rh, Pd, Cu, Nb, Ni, V, and Ir, exhibit endergonic free energy changes below 0.7 eV for this step. In contrast, the process is exergonic for p-block metals, except for aluminum (Al), as well as for pseudo p-block metals and late transition metals such as Ag, Au, and Pt. A notable exception among p-block metals is aluminum, which shows a larger endergonicity for this step, primarily due to the greater stability of the NH_2* species on aluminum nanoclusters.

Rate limiting potentials (RLP). In the previous section, we provided a comprehensive analysis of the adsorption free energies for various nitrogen reduction reaction (NRR) intermediates, alongside the corresponding exergonic and endergonic free energy changes for each electrochemical step. The analysis revealed a general trend where adsorption free energies are significantly higher for early transition metals (TMs) and decrease progressively as one moves from early TMs to mid TMs, and further to late TMs. Early TMs display strong favorable adsorption energies for nearly all NRR intermediates, with the exception of NH_2NH_2*. Mid TMs typically show moderate to mildly favorable adsorption energies for most intermediates, though a few instances exhibit slightly positive, unfavorable adsorption energies. In contrast, late TMs generally demonstrate unfavorable adsorption energies, either as positive values or very weak negative values. P-Block and pseudo p-block metals, in general, exhibit highly unfavorable, positive adsorption energies across most intermediates. Interestingly, aluminum (Al) diverges from the typical behavior of other p-block metals, displaying characteristics more similar to early transition metals (TMs) across multiple electrochemical steps. Like early TMs, which tend to have higher adsorption energies than mid or late TMs, Al shows comparatively larger adsorption free energies relative to other p-block metals. Among all intermediates, NH_2NH_2* is found to be the least stable, with positive, unfavorable adsorption energies on all nanoclusters, except for those involving manganese (Mn) and rhodium (Rh).

We have further conducted a comprehensive examination of five distinct electrochemical pathways (I to V) involved in the NRR mechanism. Table 1 provides a comprehensive analysis of the NRR mechanisms across various metal nanoclusters, identifying the lowest potential pathways along with their corresponding rate-limiting potentials (RLP) in Volts (V) and rate-limiting step. Fig. 8(a) illustrates the RLP for different nanoclusters, revealing clear trends in RLP.

With few exceptions—such as Cr, Mn, Tc, Re, and Hg—all metal nanoclusters predominantly favor the alternative-distal mixed pathway (Path IV) as their most preferred mechanism, with the alternative pathway (Path V) following closely as the second choice. The distal pathways are generally less favored, typically ranking from third to fifth, with the predominant order for distal mechanism being Path I < Path II < Path III. This trend suggests a general preference for the reaction pathway involving the NHNH* intermediate. However, Cr, Mn, Tc, and Re diverge from this pattern by favoring Path I, which follows the distal mechanism, indicating a distinct catalytic behavior for these metals. Hg stands out as the only metal preferring the alternative mechanism (Path V), although it exhibits unfavorable adsorption energies across all species, making this metal less effective for catalysis.

The nitrogen reduction reaction (NRR) on metal and metal oxide surfaces typically considers the distal and alternating pathways. However, for nanoclusters, we have identified that the alternative-distal mixed pathway (Path IV: * + N_2 → NNH* → NHNH* → $NHNH_2$* → NH* → NH_2* → *) is the preferred mechanism. This finding emphasizes the need to account for mixed pathways, which are often overlooked in favor of the more conventional distal (Path I) and alternating (Path V) pathways in NRR studies.

In terms of the rate-limiting steps (RLP), early and mid-transition metals, including Al from the p-block, predominantly experience their rate-limiting step during the sixth electrochemical step, NH_2* → NH_3(g) + *. This step is crucial as it involves the regeneration of the nanocluster surface by removing the NH_2* adsorbate, which is vital for the continuation of the catalytic cycle.

On the other hand, late transition metals and p-block metals (excluding Al) and pseudo-P block metals exhibit a shift in their rate-limiting step to the first hydrogenation step, * + N_2* → NNH*, indicating a complete reversal from the last step to the first. This suggests that for these metals, the initial activation of nitrogen and its conversion to NNH* is the most energetically challenging step, thus setting the pace for the entire reaction process.

There are notable exceptions to these general trends. For example, niobium (Nb), among the mid-transition metals, displays a unique reaction limiting potential (RLP) during the

Table 1 Most preferred pathways (lowest 1 to 5), rate-limiting potentials (RLP) in Volts (V) and corresponding steps for the lowest energy pathway for NRR and HER, along with the relative preference between NRR and HER based on their differences

	Path preference (rank 1 to 5)						RLP (in V)		
Metal	1	2	3	4	5	RL step	NRR	HER	(NRR-HER)
Sc	IV	V	I	II	III	$NH_2^* \rightarrow NH_3(g) + *$	1.55	0.97	0.58
Ti	IV	V	I	II	III	$NH_2^* \rightarrow NH_3(g) + *$	1.48	0.90	0.58
V	IV	V	I	II	III	$NH_2^* \rightarrow NH_3(g) + *$	0.63	0.13	0.51
Cr	I	II	III	IV	V	$NH_2^* \rightarrow NH_3(g) + *$	0.89	0.36	0.53
Mn	I	II	III	IV	V	$NH_2^* \rightarrow NH_3(g) + *$	0.94	1.24	−0.29
Fe	IV	V	I	II	III	$NH_2^* \rightarrow NH_3(g) + *$	1.02	0.46	0.55
Co	IV	V	I	II	III	$NH_2^* \rightarrow NH_3(g) + *$	1.06	0.46	0.61
Ni	IV	V	I	II	III	$* + N_2^* \rightarrow NNH^*$	0.56	0.20	0.36
Cu	IV	V	II	III	I	$* + N_2^* \rightarrow NNH^*$	1.33	0.03	1.30
Zn	IV	V	II	III	I	$* + N_2^* \rightarrow NNH^*$	2.15	0.36	1.79
Y	IV	V	I	II	III	$NH_2^* \rightarrow NH_3(g) + *$	1.70	1.02	0.68
Zr	IV	V	I	II	III	$NH_2^* \rightarrow NH_3(g) + *$	1.33	0.89	0.44
Nb	IV	V	I	II	III	$NNH_2^* \rightarrow NHNH_2^*$	0.48	0.20	0.28
Mo	IV	V	I	II	III	$NH_2^* \rightarrow NH_3(g) + *$	0.83	0.27	0.56
Tc	I	II	III	IV	V	$NH_2^* \rightarrow NH_3(g) + *$	1.28	0.90	0.38
Ru	IV	V	II	III	I	$NH_2^* \rightarrow NH_3(g) + *$	0.85	0.59	0.26
Rh	IV	V	I	II	III	$NH_2^* \rightarrow NH_3(g) + *$	0.23	0.32	−0.09
Pd	IV	V	I	II	III	$NH_2^* \rightarrow NH_3(g) + *$	0.31	0.46	−0.16
Ag	IV	V	II	III	I	$* + N_2^* \rightarrow NNH^*$	2.07	0.40	1.67
Cd	IV	V	II	III	I	$* + N_2^* \rightarrow NNH^*$	2.19	0.80	1.38
Hf	IV	V	I	II	III	$NNH^* \rightarrow NHNH^*$	1.40	0.83	0.58
Ta	IV	V	I	II	III	$NH_2^* \rightarrow NH_3(g) + *$	0.97	0.18	0.80
W	IV	V	I	II	III	$NH_2^* \rightarrow NH_3(g) + *$	1.72	0.95	0.77
Re	I	II	III	IV	V	$NH_2^* \rightarrow NH_3(g) + *$	1.38	0.26	1.12
Os	IV	V	I	II	III	$NH_2^* \rightarrow NH_3(g) + *$	1.26	0.70	0.56
Ir	IV	V	I	II	III	$NH_2^* \rightarrow NH_3(g) + *$	0.70	0.66	0.04
Pt	IV	V	I	II	III	$* + N_2^* \rightarrow NNH^*$	0.70	0.12	0.58
Au	IV	V	II	III	I	$* + N_2^* \rightarrow NNH^*$	1.80	0.06	1.74
Hg	V	IV	III	II	I	$* + N_2^* \rightarrow NNH^*$	2.18	1.69	0.49
Al	IV	V	I	II	III	$NH_2^* \rightarrow NH_3(g) + *$	1.04	0.21	0.83
Ga	IV	V	I	II	III	$* + N_2^* \rightarrow NNH^*$	1.69	0.13	1.57
In	IV	V	I	II	III	$* + N_2^* \rightarrow NNH^*$	1.92	0.48	1.44
Tl	IV	V	I	II	III	$* + N_2^* \rightarrow NNH^*$	1.93	0.40	1.53
Sn	IV	V	I	II	III	$* + N_2^* \rightarrow NNH^*$	2.37	0.88	1.49
Pb	IV	V	I	II	III	$* + N_2^* \rightarrow NNH^*$	2.28	0.82	1.46
Bi	IV	V	I	II	III	$* + N_2^* \rightarrow NNH^*$	2.36	0.55	1.81

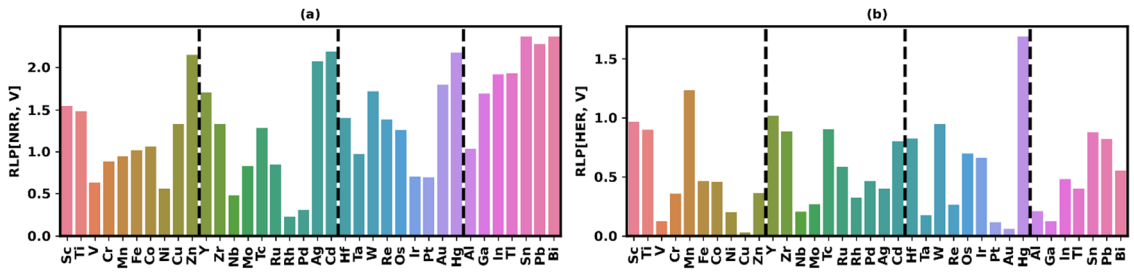

Fig. 8 Rate-limiting potentials (RLP) for (a) the nitrogen reduction reaction (NRR) and (b) the hydrogen evolution reaction (HER) in volts (V).

$NNH_2^* \rightarrow NHNH_2^*$ step. Similarly, hafnium (Hf), an early transition metal, shows its RLP during the $NNH^* \rightarrow NHNH^*$ transition, suggesting that this specific step is particularly challenging for Hf nanoclusters.

Overall, the analysis reveals that the preference for reaction pathways and rate-limiting steps in the NRR is significantly influenced by the type of metal and its position in the periodic table. Early and mid-transition metals, along with Al, tend to have their catalytic efficiency dictated by the final nanocluster regeneration step, while late transition metals and most p-block metals focus on the initial nitrogen activation step. The exceptions observed in Nb and Hf highlight the diversity in catalytic behavior across different metals, emphasizing the need for tailored approaches when designing nanocluster catalysts for efficient NRR. This nuanced understanding of pathway preferences and rate-limiting steps provides valuable insights that can drive the development of next-generation catalysts for sustainable ammonia production.

Fig. 9 highlights the efficiency of various metal nanoclusters for the nitrogen reduction reaction (NRR) by displaying their

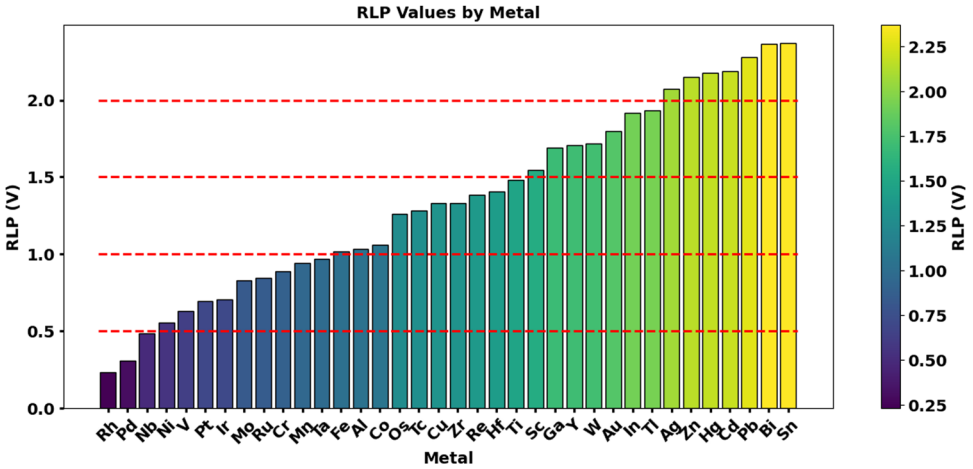

Fig. 9 Rate-limiting potentials (RLP in V) by metal, ordered in ascending order. The red dashed lines indicate key RLP thresholds across different metals. The color gradient represents the RLP values, with lower values in purple and higher values in yellow, showing the relative differences in RLP across various metals.

rate-limiting potential (RLP) values in ascending order. Rhodium (Rh) stands out with the lowest RLP of 0.23 V, indicating its superior catalytic efficiency for NRR, as it requires the least potential to drive the rate-limiting step. Following closely, palladium (Pd) and niobium (Nb) also demonstrate high efficiency with RLP values of 0.31 V and 0.48 V, respectively, suggesting that these metals are also highly effective catalysts for NRR.

In addition to these top performers, a group of metal nanoclusters, including nickel (Ni), vanadium (V), platinum (Pt), iridium (Ir), molybdenum (Mo), ruthenium (Ru), chromium (Cr), manganese (Mn), tantalum (Ta), iron (Fe), aluminium (Al) and cobalt (Co) all exhibit RLP values around or below 1.0 V. This range of values suggests that these metals are relatively efficient for NRR, as they require a moderate potential to overcome the rate-limiting step. Their lower RLPs indicate a balance between the energy required to drive the reaction and the stability of the intermediate species involved, making them viable candidates for NRR catalysis.

The rate-limiting potential (RLP) serves as a key descriptor for evaluating the catalytic efficiency of different nitrogen reduction reaction (NRR) catalysts. However, direct comparisons between different catalyst systems—such as nanoclusters, single-atom catalysts (SACs), double-atom catalysts (DACs), core–shell nanoalloys, and size-selected clusters—are challenging due to fundamental differences in their electronic structures, coordination environments, and stabilization mechanisms.[105–115]

For instance, Fe single-atom catalysts on $TiO_2(001)$ exhibit an RLP of 1.27 V, which is slightly higher than the Fe nanocluster (1.02 V) studied here.[105] This suggests that Fe nanoclusters may exhibit improved catalytic performance in some cases, but SACs on oxide supports can provide enhanced stability and selectivity. Similarly, Yang *et al.* reported an RLP of 0.58 V for $Ni_{13}/TiO_2(101)$, which is remarkably close to our reported 0.56 V for free-standing Ni_{10} nanoclusters, indicating that larger Ni clusters behave similarly in supported and unsupported environments.[109] However, for small nanoclusters (Ni_4/TiO_2), Yang *et al.* observed a much lower RLP of 0.33 V, demonstrating that reducing cluster size can significantly alter catalytic behavior.

Beyond size effects, composition plays a crucial role in tuning the RLP. Chen *et al.* screened a large number of three-metal clusters embedded in a two-dimensional metal nitride (W_2N_3) with a nitrogen vacancy and found that the VNiCu cluster exhibits a wide range of RLP values from 0.37 V to 1.43 V, depending on the specific metal composition.[108] This demonstrates that size-selected clusters and multi-metallic compositions introduce strong variations in NRR activity, making general comparisons difficult. A similar trend was observed by Li *et al.*, who predicted that Fe&Ni@Mo_2CS_2 diatomic catalysts exhibit exceptional NRR performance, with an RLP as low as 0.48 V.[115] Their study attributed this to the efficient combination of Fe in a high-spin state and Ni in a low-spin state, which facilitates nitrogen activation and ammonia desorption. Das *et al.* investigated core–shell iron nanoalloy catalysts $M_{15}@Fe_{50}$, where M = Co, Ni, Cu and reported varying RLP values of 0.33 V (Co@Fe), 0.94 V (Ni@Fe), and 0.27 V (Cu@Fe).[113] Interestingly, our reported RLP for Ni_{10} nanoclusters closely matches the value for $Ni_{15}@Fe_{50}$, suggesting that in certain cases, isolated nanoclusters and core–shell systems may exhibit similar trends.

Perhaps the most striking deviation arises when comparing nanoclusters with double-atom catalysts (DACs). Rasool *et al.* reported extremely low RLP values of −0.56 V, −0.58 V, and −0.53 V for Fe_2, Co_2, and W_2 DACs, impregnated in a tetracyanoquinodimethane-based monolayer respectively.[110] These values differ significantly from our reported RLP values for 10-atom clusters of the same metals. This suggests that DACs and nanocluster-based catalysts do not behave similarly, as the presence of additional metal atoms in nanoclusters leads to different electronic environments, coordination effects, and reaction mechanisms compared to DACs.

Our findings, in conjunction with recently reported RLP values, highlight that direct comparisons between different catalyst systems must be approached with caution. Nanoclusters,

single-atom catalysts, double-atom catalysts, core–shell alloys, and multi-metal nanoalloys all exhibit distinct electronic properties and stabilization mechanisms, leading to substantial variations in RLP values. While trends can be drawn within a specific class of catalysts, one-to-one comparisons across different catalyst architectures can be misleading. Future studies should focus on systematically correlating catalyst size, composition, and support effects to better understand the design principles governing NRR efficiency across various catalytic architectures.

NRR *vs.* HER

One of the major challenges in the electrochemical nitrogen reduction reaction (NRR) is the competing hydrogen evolution reaction (HER), which can significantly compromise both the selectivity and efficiency of NH_3 production. Since NRR and HER occur at similar potentials, HER often dominates due to its faster kinetics, particularly in aqueous environments where protons are abundant. This competition typically results in the majority of electrons being consumed for H_2 evolution rather than N_2 reduction, making the suppression of HER crucial for enhancing NRR selectivity.

Fig. 7(b) depicts the free energy changes for H* desorption across different nanoclusters, and Fig. 8(b) displays the rate-limiting potentials (RLP) for the hydrogen evolution reaction (HER). The desorption step is observed to be endergonic on most nanoclusters, with the exception of p-block metals (excluding Al), pseudo-p-block metals, and Ag. Based on the values of RLP(NRR)–RLP(HER) presented in Table 1, where a negative value indicates a stronger selectivity towards NRR over HER, certain metals exhibit promising performance. Specifically, Mn (−0.29 eV), Pd (−0.16 eV), and Rh (−0.09 eV) show a clear preference for NRR, suggesting that these metals are more selective for nitrogen reduction under the studied conditions. In contrast, Ir (0.0428) demonstrates a slight preference for HER, but the minimal difference between NRR and HER activity suggests it could potentially be optimized for NRR. Other metals such as Ru (0.26 eV) and Nb (0.28 eV) show a moderate preference for HER, with small but positive values indicating a more competitive balance between the two reactions. -0.00w?>However, the remaining metals exhibit a much stronger inclination towards HER, with values greater than 0.35 eV, indicating significant challenges in using these metals for NRR. These insights are critical for guiding the design and selection of electrocatalysts aimed at improving the selectivity and efficiency of NRR in future studies.

Charge analysis

In Fig. 10, we present the correlation between the adsorption free energies of various intermediates in the nitrogen reduction reaction (NRR) and the corresponding residual Bader charges on these adsorbates across different metal categories, including early TMs, mid TMs, Late TMs, p-block metals, and pseudo-p block metals. Fig. S1 (ESI†) provides detailed plots of the residual Bader charges for each NRR adsorbate across all nanoclusters.

Our analysis reveals that a strong correlation between residual charges on adsorbates and their respective adsorption free energies is not universally observed. The most pronounced correlation is seen with the N_2* adsorbate ($R = -0.87$), followed by NNH* ($R = -0.77$), whereas NH_2NH_2* shows no significant correlation. These negative correlations suggest that increased electron density, indicative of greater electron transfer from the nanocluster to the adsorbate, generally results in greater stabilization of the adsorbate, reflected in more negative adsorption free energy values.

The plots demonstrate a significant electron transfer from the nanocluster moiety to the adsorbate, particularly for early TMs, which show notably larger adsorption free energies. For example, the residual electron densities on the N_2* adsorbate are approximately $1.9e^-$ on Sc and $1.7e^-$ on Ti nanoclusters, indicating substantial electron transfer from the cluster to the adsorbate, with roughly $1e^-$ transferred to each nitrogen atom.

Further examination reveals that early TMs consistently exhibit high electron density on the adsorbates, correlating with stronger adsorption energies. This suggests that early TMs effectively facilitate charge transfer to the adsorbates, thereby stabilizing them more robustly. As we progress from early to late TMs, there is a noticeable decline in both the residual charge on the adsorbates and the adsorption energies, indicating a reduced ability of the metal clusters to donate electrons to the adsorbates, resulting in weaker adsorption.

When we narrow our analysis to early, mid, and late transition metals (excluding p-block and pseudo-p-block metals), as shown in Fig. S2 (ESI†), the correlation coefficients improve for all adsorbates, ranging from −0.80 to −0.86, with the exceptions of NH_2* ($R = -0.66$), $NHNH_2$* ($R = -0.63$), and NH_2NH_2* ($R = 0.09$). This indicates that the inclusion of p- and pseudo p-block metals reduces the observed correlation between adsorption free energies and residual charges on adsorbates.

Interestingly, p-block and pseudo p-block metals generally display moderate to large residual charges on adsorbates across most nanoclusters, except for the N_2* and NH_2NH_2* intermediates. Notably, N_2* does not exhibit adsorption on most p-block and pseudo-p block metal nanoclusters, with the exception of Al, where a bond with N_2* is formed, as reflected in a Bader charge density of $0.41e^-$.

Despite the moderate to large electron transfer observed for adsorbates on p-block and pseudo-p block metals, the adsorption free energies are generally unfavorable. For instance, NNH* on Ga, In, and Tl nanoclusters shows residual charges of $0.98e^-$, $0.85e^-$, and $0.63e^-$, respectively, yet the adsorption free energies remain positive and unfavorable, with values of 1.69 eV, 1.91 eV, and 1.93 eV, respectively. Aluminum shows a significantly larger electron density transfer to NNH* ($2.22e^-$), but the adsorption energy is only slightly favorable at −0.10 eV. Similar observations hold true for other intermediates. This suggests that for p-block and pseudo-p block metals, there is no clear correlation between residual charges and adsorption free energies.

HOMO–LUMO gap

Fig. S3 (ESI†) presents the HOMO–LUMO gaps for various adsorbates across different nanocluster surfaces, and no clear

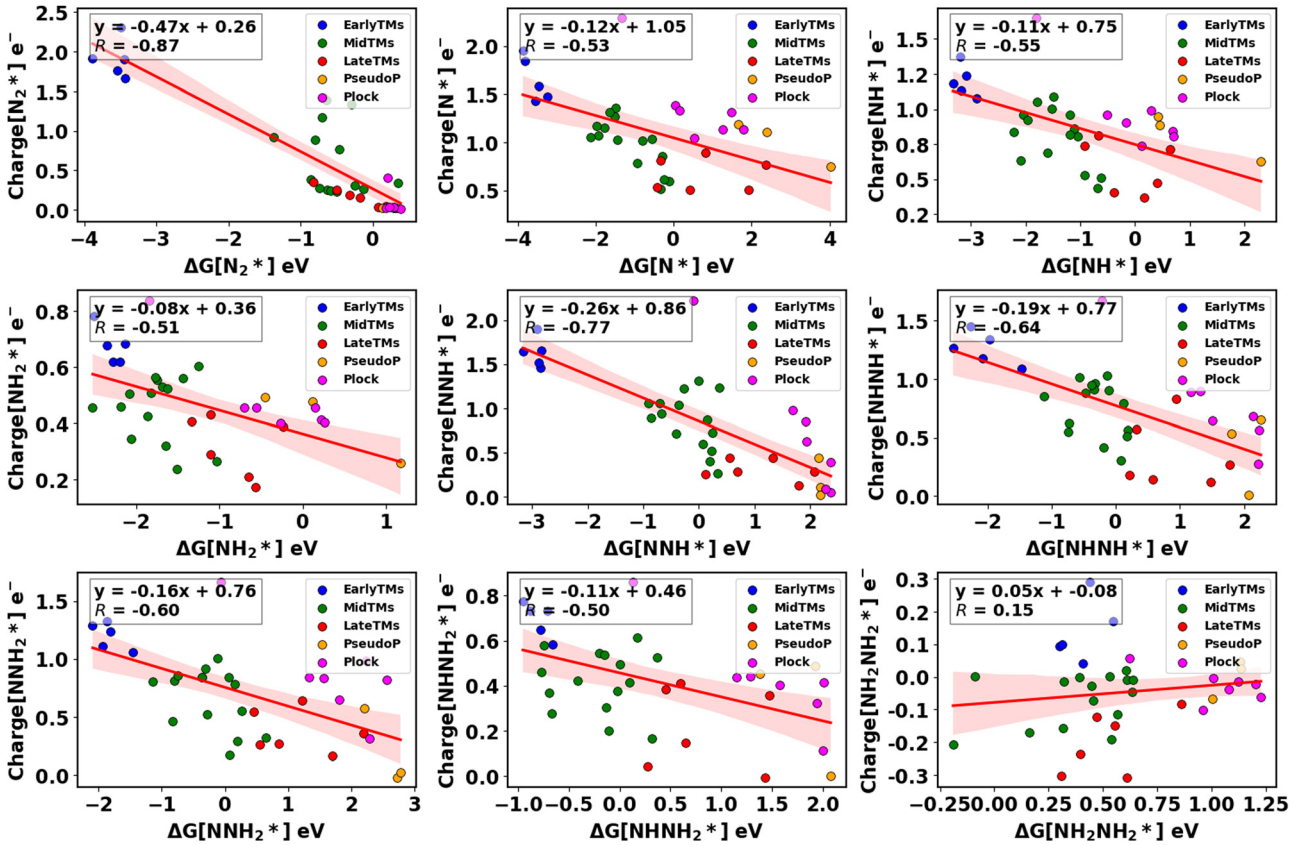

Fig. 10 Correlation between adsorption free energies (ΔG), (eV) and residual Bader charges (e^-) on adsorbates for various adsorbates during the nitrogen reduction reaction (NRR) across different categories of metals. The red lines show linear regressions, with R values indicating the strength of correlation.

correlation is observed between the adsorption free energies of the adsorbates and the corresponding HOMO–LUMO gaps. For example, the HOMO–LUMO gap for the NNH* adsorbate on early transition metals (TMs) ranges from 0.20 eV to 0.26 eV, while the adsorption free energies span from −3.16 eV to −2.83 eV. In contrast, transition metals such as Co, Mo, and Rh exhibit similar HOMO–LUMO gaps (0.21 eV to 0.24 eV), but their adsorption free energies are unfavorable, with values of 0.08 eV, 0.14 eV, and 0.20 eV, respectively. Additionally, metals such as Re, Os, and Tc, which display smaller HOMO–LUMO gaps (0.13 eV to 0.24 eV), show much more favorable adsorption free energies of −0.86 eV, −0.41 eV, and −0.68 eV, respectively. Similar trends are observed for other nitrogen reduction reaction (NRR) adsorbates as well.

In the global minimum configurations, the HOMO–LUMO gap increases for the first 10 metal nanoclusters in the order of Ru < Mn < Ir < Cr < W < Pd < Y < Rh < Ti < Co, with values ranging from 0.02 eV to 0.15 eV. However, the free energy change for the first electrochemical step leading to the formation of NNH* from the global minimum configuration (* + N_2* → NNH*) exhibits both exergonic and endergonic values, ranging from −2.90 eV to 0.36 eV. This suggests that there is no direct relationship between the HOMO–LUMO gap and the exergonicity or endergonicity associated with each electrochemical step. Similar observations hold true for other adsorbates.

A broader analysis reveals that p-block metals (*e.g.*, Al, Ga, In, and Tl) and pseudo-p block metals (Zn, Cd, and Hg) generally tend to exhibit significantly larger HOMO–LUMO gaps compared to most transition metals, suggesting that these nanoclusters are generally more chemically stable and less reactive. In contrast, transition metals, particularly those from the early and mid-transition series (*e.g.*, Ti, Cr, Fe, and Ni), tend to display smaller HOMO–LUMO gaps, which correlates with higher chemical reactivity and catalytic potential. Late transition metals, including Cu, Ag, and Au, exhibit relatively larger HOMO–LUMO gaps, indicating lower catalytic activity. Furthermore, metals with a d^3 configuration, such as Ti, Nb, and Ta, show larger HOMO–LUMO gaps for many adsorbates compared to other early or mid-transition metals within the 3d, 4d, and 5d blocks, respectively. Similarly, late transition metals with a d^9 configuration, such as Cu, Ag, and Au, generally display larger HOMO–LUMO gaps. These observations suggest that no clear trend can be established between adsorption free energies and HOMO–LUMO gap values.

Scaling relationships

The heatmap in Fig. 11 offers a comprehensive visual representation of the correlation coefficients between the adsorption free energies (ΔG) of various intermediates involved in the nitrogen reduction reaction (NRR). Fig. 12 highlights the

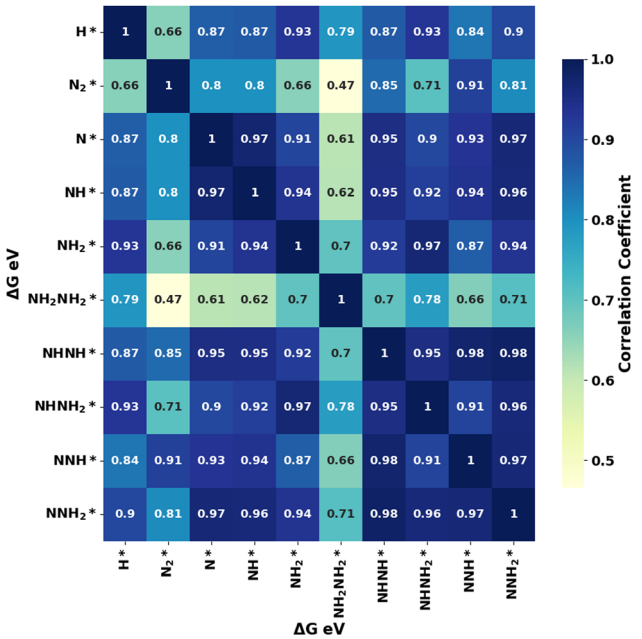

Fig. 11 Heatmap illustrating the correlation between the adsorption free energies (ΔG) of various intermediates in the nitrogen reduction reaction (NRR).

specific correlation between the adsorption free energy of NH* and other key intermediates. Additionally, the correlation plots between the adsorption free energies of N* and N_2* are shown in Fig. S4 and S5 in the ESI.†

A key observation from the heatmap is the strong linear scaling relationships among many of the intermediates involved in the NRR patways. For instance, the correlations between intermediates such as N*, NH*, NH_2*, NNH*, NHNH*, NNH_2*, and $NHNH_2$* are notably high, with coefficients ranging from 0.87 to 0.98. Except for a single case involving the correlation between NH_2* and NNH*, where the coefficient is slightly lower, all other values exceed 0.90. This consistency indicates that catalysts that favorably bind one of these intermediates are likely to similarly favor the binding of others, following a predictable linear trend. These strong correlations imply that the adsorption energies of these species are governed by similar surface interactions and electronic factors, making the optimization of catalysts more straightforward when focusing on these intermediates.

In contrast, the intermediate NH_2NH_2* exhibits weaker correlations with other species, indicating that its adsorption energy does not scale as predictably with other NRR intermediates. This deviation suggests that NH_2NH_2* may involve more complex interactions with the catalytic surface, likely due to a different electronic environment or distinct binding modes. One possible reason for this deviation is that NH_2NH_2* has a

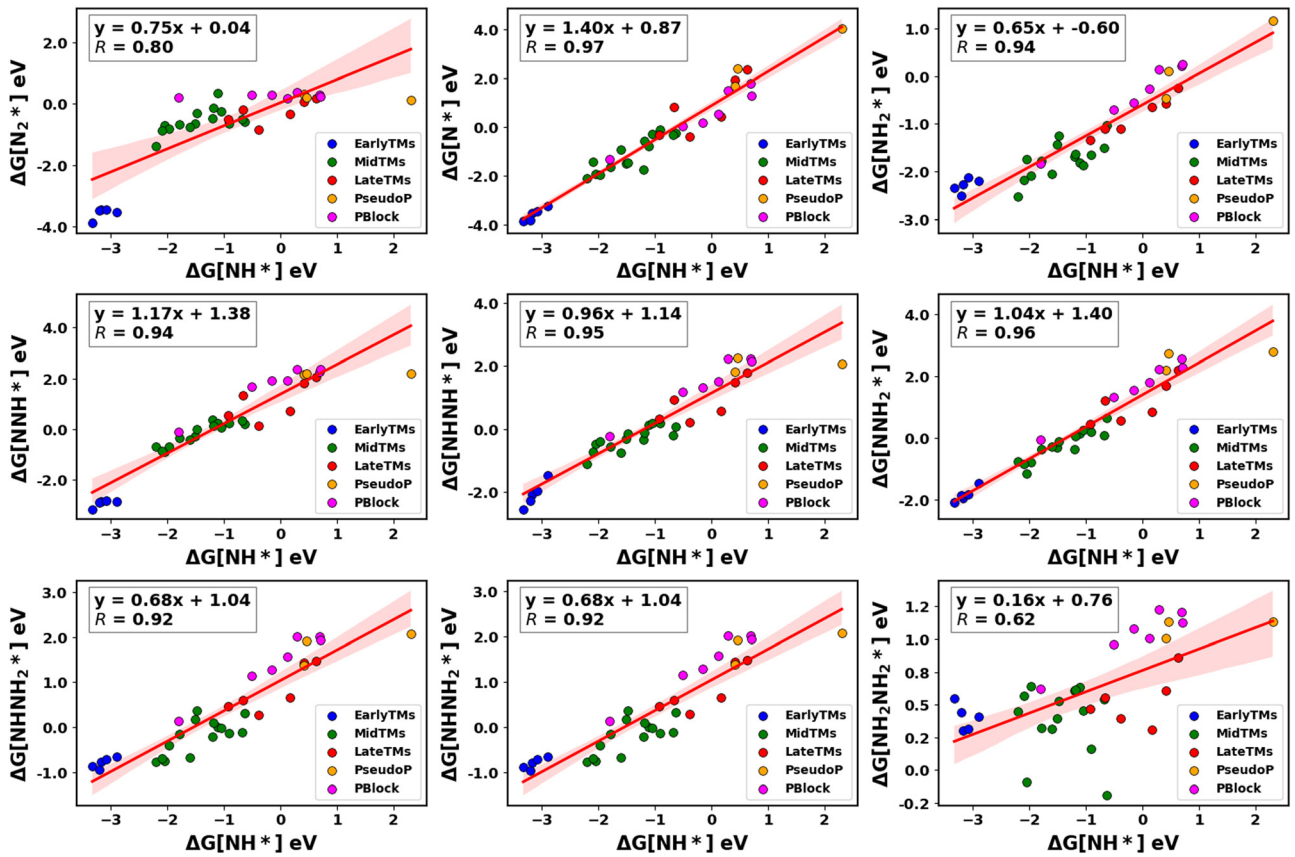

Fig. 12 Correlation plot showing the relationship between the adsorption free energies (ΔG) of NH* and other adsorbates in the nitrogen reduction reaction (NRR).

fully saturated bonding pattern, which differs significantly from other intermediates that typically have at least one bonding site open for further coordination. This unique bonding configuration may result in distinct adsorption behavior, necessitating specialized considerations in catalyst design.

The adsorption free energies of N_2* do not correlate well with the intermediates involved in the NRR mechanism (see Fig. S5, ESI†). Although N_2* exhibits a stronger correlation with NNH* (0.91), it shows only moderate correlations with intermediates such as N*, NH*, NHNH*, and NNH_2*, with coefficients ranging from 0.80 to 0.85. Additionally, N_2* displays even weaker correlations with NH_2* (0.66), $NHNH_2$* (0.71) and NH_2NH_2* (0.47). These weaker correlations indicate that the binding of N_2* is not a reliable descriptor for the NRR mechanism, as it may be influenced by different surface characteristics or adsorption sites compared to those affecting the binding of other intermediates. Therefore, it is more effective to include intermediates directly involved in the NRR mechanism as descriptors when optimizing nanocluster surfaces for enhanced NRR performance.

Conclusions

In this study, we have conducted a comprehensive DFT investigation into the electrocatalytic reduction of nitrogen (N_2) to ammonia (NH_3) on d-block and p-block metal nanoclusters, elucidating key trends and notable exceptions arising from geometric changes during the formation of intermediates. These exceptions are particularly evident when intermediates deviate from their global minimum (GM) configurations. The key findings of this study are summarized as follows:

– Adsorption free energies for nearly all NRR intermediates exhibit significantly larger negative values for early transition metals (TMs), which progressively decrease from early TMs to mid and late TMs.

– Early TMs show strong favorable adsorption for most NRR intermediates, except for NH_2NH_2*, which remains unstable. Mid TMs exhibit mild to moderately favorable adsorption free energies, with some exceptions displaying mildly unfavorable positive free energies. Late TMs generally show unfavorable positive or only slightly favorable negative adsorption free energies for most intermediates.

– P-Block and pseudo-p block metals exhibit highly unfavorable positive adsorption energies, limiting their catalytic efficacy. However, aluminum (Al) exhibits electrochemical behavior that somewhat resembles early TMs in several key electrochemical steps, making it a unique p-block metal in this regard.

– NH_2NH_2* is identified as the least stable intermediate, with unfavorable adsorption free energies on nearly all nanoclusters, except for manganese (Mn) and rhodium (Rh).

– In the second electrochemical step, the formation of NHNH* from NNH* is favored over NNH_2*, while in the third step, N* is preferred over $NHNH_2$*, and in the fourth step, NH* is more stable than NH_2NH_2*.

– The alternative-distal mixed pathway (Path IV) is identified as the preferred mechanism for nanoclusters in the NRR, emphasizing the need to consider mixed pathways, often overlooked in favor of conventional distal and alternating pathways in electrochemical NRR studies.

– Rhodium (Rh) demonstrates the highest catalytic efficiency, with the lowest rate-limiting potential (RLP) of 0.23 V. Palladium (Pd) and niobium (Nb) also show high efficiency, with RLP values of 0.31 V and 0.48 V, respectively. Several other metals, including nickel (Ni), vanadium (V), platinum (Pt), iridium (Ir), molybdenum (Mo), and manganese (Mn), exhibit RLP values around or below 1.0 V, indicating moderate efficiency.

– Manganese (Mn), palladium (Pd), and rhodium (Rh) show moderate selectivity for nitrogen reduction over the competing hydrogen evolution reaction (HER), making them promising candidates for efficient NRR catalysis.

– Strong linear scaling relationships were identified among key NRR intermediates, such as N*, NH*, NH_2*, NNH*, NHNH*, and NNH_2*, indicating that stabilizing one intermediate often stabilizes others, aiding in catalyst optimization.

– Charge analysis reveals that a strong correlation between the residual charges on adsorbates and their respective adsorption free energies is not consistently observed.

– No clear correlation was found between the HOMO–LUMO gaps of nanocluster surfaces and the adsorption free energies of NRR intermediates, suggesting that other factors contribute to catalytic behavior.

Overall, this study provides valuable insights into the catalytic performance of d- and p-block metal nanoclusters for the nitrogen reduction reaction, offering guidance for future catalyst design and optimization efforts in sustainable ammonia production.

This study focuses exclusively on 10-atom nanoclusters, and the findings are not directly scalable to significantly larger nanoclusters due to quantum size effects, which can substantially alter electronic and catalytic properties. However, these results are particularly relevant for size-selected nanoclusters, where precise control over cluster size allows for targeted catalytic performance. While our findings provide valuable insights into nitrogen reduction on small nanoclusters, we acknowledge that larger clusters may exhibit different trends. Future studies should explore the impact of cluster size scaling to better understand how catalytic behavior evolves with increasing cluster size. This study provides significant fundamental insights into the trends in NRR performance across different nanoclusters, depending on whether they belong to 3d, 4d, 5d, or p-block metals, thereby facilitating the strategic design of stable and efficient electrocatalysts, particularly for size-selected small nanocluster-based electrocatalysis applications.

Data availability

The data supporting this article have been included as part of the ESI.† The coordinates of all geometries, including global

minimum configurations and cluster-bound adsorbates are given in the Appendix section of the ESI.†

Conflicts of interest

There are no conflicts to declare.

Acknowledgements

RKR would like to thank the University of Birmingham's BlueBEAR HPC facility (**https://www.bear.bham.ac.uk/bluebear**) for providing computational resources and support.

References

1 J. N. Galloway, A. R. Townsend, J. W. Erisman, M. Bekunda, Z. Cai, J. R. Freney, L. A. Martinelli, S. P. Seitzinger and M. A. Sutton, Transformation of the Nitrogen Cycle: Recent Trends, Questions, and Potential Solutions, *Science*, 2008, **320**(5878), 889–892, DOI: **10.1126/science.1136674**.

2 C. Zamfirescu and I. Dincer, Using Ammonia as a Sustainable Fuel, *J. Power Sources*, 2008, **185**(1), 459–465, DOI: **10.1016/j.jpowsour.2008.02.097**.

3 I. A. Amar, R. Lan, C. T. G. Petit and S. Tao, Solid-State Electrochemical Synthesis of Ammonia: A Review, *J. Solid State Electrochem.*, 2011, **15**(9), 1845–1860, DOI: **10.1007/s10008-011-1376-x**.

4 S. Giddey, S. P. S. Badwal and A. Kulkarni, Review of Electrochemical Ammonia Production Technologies and Materials, *Int. J. Hydrogen Energy*, 2013, **38**(34), 14576–14594, DOI: **10.1016/j.ijhydene.2013.09.054**.

5 H. Liu, Ammonia Synthesis Catalyst 100 Years: Practice, Enlightenment and Challenge, *Cuihua Xuebao*, 2014, **35**(10), 1619–1640, DOI: **10.1016/S1872-2067(14)60118-2**.

6 H. Jin, S. S. Kim, S. Venkateshalu, J. Lee, K. Lee and K. Jin, Electrochemical Nitrogen Fixation for Green Ammonia: Recent Progress and Challenges, *Adv. Sci.*, 2023, **10**(23), 1–20, DOI: **10.1002/advs.202300951**.

7 G. Qing, R. Ghazfar, S. T. Jackowski, F. Habibzadeh, M. M. Ashtiani, C.-P. Chen, M. R. Smith and T. W. Hamann, Recent Advances and Challenges of Electrocatalytic N_2 Reduction to Ammonia, *Chem. Rev.*, 2020, **120**(12), 5437–5516, DOI: **10.1021/acs.chemrev.9b00659**.

8 H. Shen, C. Choi, J. Masa, X. Li, J. Qiu, Y. Jung and Z. Sun, Electrochemical Ammonia Synthesis: Mechanistic Understanding and Catalyst Design, *Chem*, 2021, **7**(7), 1708–1754, DOI: **10.1016/j.chempr.2021.01.009**.

9 Q. Liu, T. Xu, Y. Luo, Q. Kong, T. Li, S. Lu, A. A. Alshehri, K. A. Alzahrani and X. Sun, Recent Advances in Strategies for Highly Selective Electrocatalytic N_2 Reduction toward Ambient NH_3 Synthesis, *Curr. Opin. Electrochem.*, 2021, **29**, 100766, DOI: **10.1016/j.coelec.2021.100766**.

10 X. Cui, C. Tang and Q. Zhang, A Review of Electrocatalytic Reduction of Dinitrogen to Ammonia under Ambient Conditions, *Adv. Energy Mater.*, 2018, **8**, 1800369, DOI: **10.1002/aenm.201800369**.

11 N. Zhang, L. Li, J. Wang, Z. Hu, Q. Shao, X. Xiao and X. Huang, Surface-Regulated Rhodium–Antimony Nanorods for Nitrogen Fixation, *Angew. Chem., Int. Ed.*, 2020, **59**(21), 8066–8071, DOI: **10.1002/anie.201915747**.

12 W. Li, K. Li, Y. Ye, S. Zhang, Y. Liu, G. Wang, C. Liang, H. Zhang and H. Zhao, Efficient Electrocatalytic Nitrogen Reduction to Ammonia with Aqueous Silver Nanodots, *Commun. Chem.*, 2021, **4**(1), 1–11, DOI: **10.1038/s42004-021-00449-7**.

13 N. Zhang, F. Zheng, B. Huang, Y. Ji, Q. Shao, Y. Li, X. Xiao and X. Huang, Exploring Bi2Te3 Nanoplates as Versatile Catalysts for Electrochemical Reduction of Small Molecules, *Adv. Mater.*, 2020, **32**(22), 1–9, DOI: **10.1002/adma.201906477**.

14 R. Amrine, M. A. Montiel, V. Montiel and J. Solla-Gullón, Evaluation of Pt–Rh Nanoparticle–Based Electrodes for the Electrochemical Reduction of Nitrogen to Ammonia, *Electrocatalysis*, 2024, **15**(2–3), 239–250, DOI: **10.1007/s12678-024-00870-1**.

15 Y. Ding, L. Huang, J. Zhang, A. Guan, Q. Wang, L. Qian, L. Zhang and G. Zheng, Ru-Doped, Oxygen-Vacancy-Containing CeO_2 Nanorods toward N_2 Electroreduction, *J. Mater. Chem. A*, 2020, **8**(15), 7229–7234, DOI: **10.1039/D0TA02211J**.

16 H. Huang, L. Xia, X. Shi, A. M. Asiri and X. Sun, Ag Nanosheets for Efficient Electrocatalytic N_2 Fixation to NH_3 under Ambient Conditions, *Chem. Commun.*, 2018, **54**(81), 11427–11430, DOI: **10.1039/c8cc06365f**.

17 M. Shi, D. Bao, S. Li, B. Wulan, J. Yan and Q. Jiang, Anchoring PdCu Amorphous Nanocluster on Graphene for Electrochemical Reduction of N_2 to NH_3 under Ambient Conditions in Aqueous Solution, *Adv. Energy Mater.*, 2018, **8**(21), 1800124, DOI: **10.1002/aenm.201800124**.

18 J. G. Howalt and T. Vegge, Electrochemical Ammonia Production on Molybdenum Nitride Nanoclusters, *Phys. Chem. Chem. Phys.*, 2013, **15**(48), 20957–20965, DOI: **10.1039/c3cp53160k**.

19 Z. Xue, C. Sun, M. Zhao, Y. Cui, Y. Qu, H. Ma, Z. Wang and Q. Jiang, Efficient Electrocatalytic Nitrogen Reduction to Ammonia on Ultrafine Sn Nanoparticles, *ACS Appl. Mater. Interfaces*, 2021, **13**(50), 59834–59842, DOI: **10.1021/acsami.1c15324**.

20 W. Liu and J. A. Boscoboinik, FeMo Sub-Nanoclusters/Single Atoms for Neutral Ammonia Electrosynthesis, *Nano Energy*, 2020, **77**, 105078, DOI: **10.1016/j.nanoen.2020.105078**.

21 Y. Dai, Y. Wang, B. Liu and Y. Yang, Metallic Nanocatalysis: An Accelerating Seamless Integration with Nanotechnology, *Small*, 2015, **11**(3), 268–289, DOI: **10.1002/smll.201400847**.

22 N. Agarwal, V. S. Solanki, B. Pare, N. Singh and S. B. Jonnalagadda, Current Trends in Nanocatalysis for Green Chemistry and Its Applications – a Mini-Review, *Curr. Opin. Green Sustainable Chem.*, 2023, **41**, 100788, DOI: **10.1016/j.cogsc.2023.100788**.

23 Y. Du, H. Sheng, D. Astruc and M. Zhu, Atomically Precise Noble Metal Nanoclusters as Efficient Catalysts: A Bridge between Structure and Properties, *Chem. Rev.*, 2020, **120**(2), 526–622, DOI: **10.1021/acs.chemrev.8b00726**.

24 S. Lee, L. M. Molina, M. J. López, J. A. Alonso, B. Hammer, B. Lee, S. Seifert, R. E. Winans, J. W. Elam, M. J. Pellin, M. J. Pellin and S. Vajda, Selective Propene Epoxidation on Immobilized Au_{6-10} Clusters: The Effect of Hydrogen and Water on Activity and Selectivity, *Angew. Chem., Int. Ed.*, 2009, **48**(8), 1467–1471, DOI: **10.1002/anie.200804154**.

25 S. B. Somwanshi, S. B. Somvanshi and P. B. Kharat, Nanocatalyst: A Brief Review on Synthesis to Applications, *J. Phys.: Conf. Ser.*, 2020, **1644**(1), 012046, DOI: **10.1088/1742-6596/1644/1/012046**.

26 S. Vajda, M. J. Pellin, J. P. Greeley, C. L. Marshall, L. A. Curtiss, G. A. Ballentine, J. W. Elam, S. Catillon-Mucherie, P. C. Redfern, F. Mehmood, F. Mehmood and P. Zapol, Subnanometre Platinum Clusters as Highly Active and Selective Catalysts for the Oxidative Dehydrogenation of Propane, *Nat. Mater.*, 2009, **8**(3), 213–216, DOI: **10.1038/nmat2384**.

27 S. Shan, J. Luo, L. Yang and C. J. Zhong, Nanoalloy Catalysts: Structural and Catalytic Properties, *Catal. Sci. Technol.*, 2014, **4**(10), 3570–3588, DOI: **10.1039/c4cy00469h**.

28 J. Jellinek, Nanoalloys: Tuning Properties and Characteristics through Size and Composition, *Faraday Discuss.*, 2008, **138**, 11–35, DOI: **10.1039/b800086g**.

29 R. Ferrando, J. Jellinek and R. L. Johnston, Nanoalloys: From Theory to Applications of Alloy Clusters and Nanoparticles, *Chem. Rev.*, 2008, **108**(3), 845–910, DOI: **10.1021/cr040090g**.

30 X. Kang, Y. Li, M. Zhu and R. Jin, Atomically precise alloy nanoclusters: syntheses, structures, and properties, *Chem. Soc. Rev.*, 2020, **49**, 6443–6514, DOI: **10.1039/C9CS00633H**.

31 S. Ashraf, Y. Liu, H. Wei, R. Shen, H. Zhang, X. Wu, S. Mehdi, T. Liu and B. Li, Bimetallic Nanoalloy Catalysts for Green Energy Production: Advances in Synthesis Routes and Characterization Techniques, *Small*, 2023, **19**, 2303031, DOI: **10.1002/smll.202303031**.

32 G. Guisbiers, R. Mendoza-Pérez, L. Bazán-Díaz, R. Mendoza-Cruz, J. J. Velázquez-Salazar and M. José-Yacamán, Size and Shape Effects on the Phase Diagrams of Nickel-Based Bimetallic Nanoalloys, *J. Phys. Chem. C*, 2017, **121**(12), 6930–6939, DOI: **10.1021/acs.jpcc.6b09115**.

33 S. C. Jesudass, S. Surendran, J. Y. Kim, T.-Y. An, G. Janani, T.-H. Kim, J. K. Kim and U. Sim, Pathways of the Electrochemical Nitrogen Reduction Reaction: From Ammonia Synthesis to Metal-N_2 Batteries, *Electrochem. Energy Rev.*, 2023, **6**(1), 27, DOI: **10.1007/s41918-023-00186-6**.

34 M. Jiang, A. Tao, Y. Hu, L. Wang, K. Zhang, X. Song, W. Yan, Z. Tie and Z. Jin, Crystalline Modulation Engineering of Ru Nanoclusters for Boosting Ammonia Electrosynthesis from Dinitrogen or Nitrate, *ACS Appl. Mater. Interfaces*, 2022, **14**(15), 17470–17478, DOI: **10.1021/acsami.2c02048**.

35 M. Han, M. Guo, Y. Yun, Y. Xu, H. Sheng, Y. Chen, Y. Du, K. Ni, Y. Zhu and M. Zhu, Effect of Heteroatom and Charge Reconstruction in Atomically Precise Metal Nanoclusters on Electrochemical Synthesis of Ammonia, *Adv. Funct. Mater.*, 2022, **32**(29), 2202820, DOI: **10.1002/adfm.202202820**.

36 Y. Ding, L. Huang, J. Zhang, A. Guan, Q. Wang, L. Qian, L. Zhang and G. Zheng, Ru-Doped, Oxygen-Vacancy-Containing CeO_2 Nanorods toward N_2 Electroreduction, *J. Mater. Chem. A*, 2020, **8**(15), 7229–7234, DOI: **10.1039/D0TA02211J**.

37 Y. Tan, L. Yan, C. Huang, W. Zhang, H. Qi, L. Kang, X. Pan, Y. Zhong, Y. Hu and Y. Ding, Fabrication of an Au_{25}-Cys-Mo Electrocatalyst for Efficient Nitrogen Reduction to Ammonia under Ambient Conditions, *Small*, 2021, **17**(21), 2100372, DOI: **10.1002/smll.202100372**.

38 M. Shi, D. Bao, S. Li, B. Wulan, J. Yan and Q. Jiang, Anchoring PdCu Amorphous Nanocluster on Graphene for Electrochemical Reduction of N_2 to NH_3 under Ambient Conditions in Aqueous Solution, *Adv. Energy Mater.*, 2018, **8**(21), 1800124, DOI: **10.1002/aenm.201800124**.

39 M. I. Ahmed, S. Chen, W. Ren, X. Chen and C. Zhao, Synergistic Bimetallic $CoFe_2O_4$ Clusters Supported on Graphene for Ambient Electrocatalytic Reduction of Nitrogen to Ammonia, *Chem. Commun.*, 2019, **55**(81), 12184–12187, DOI: **10.1039/C9CC05684J**.

40 B. H. R. Suryanto, D. Wang, L. M. Azofra, M. Harb, L. Cavallo, R. Jalili, D. R. G. Mitchell, M. Chatti and D. R. MacFarlane, MoS_2 Polymorphic Engineering Enhances Selectivity in the Electrochemical Reduction of Nitrogen to Ammonia, *ACS Energy Lett.*, 2019, **4**(2), 430–435, DOI: **10.1021/acsenergylett.8b02257**.

41 J. Su, H. Zhao, W. Fu, W. Tian, X. Yang, H. Zhang, F. Ling and Y. Wang, Fine Rhodium Phosphides Nanoparticles Embedded in N, P Dual-Doped Carbon Film: New Efficient Electrocatalysts for Ambient Nitrogen Fixation, *Appl. Catal., B*, 2020, **265**, 118589, DOI: **10.1016/j.apcatb.2020.118589**.

42 N. Zhang, L. Li, J. Wang, Z. Hu, Q. Shao, X. Xiao and X. Huang, Surface-Regulated Rhodium–Antimony Nanorods for Nitrogen Fixation, *Angew. Chem., Int. Ed.*, 2020, **59**(21), 8066–8071, DOI: **10.1002/anie.201915747**.

43 G. Deng, T. Wang, A. A. Alshehri, K. A. Alzahrani, Y. Wang, H. Ye, Y. Luo and X. Sun, Improving the Electrocatalytic N_2 Reduction Activity of Pd Nanoparticles through Surface Modification, *J. Mater. Chem. A*, 2019, **7**(38), 21674–21677, DOI: **10.1039/C9TA06523G**.

44 W. P. Utomo, H. Wu and Y. H. Ng, Modulating the Active Sites of Oxygen-Deficient TiO_2 by Copper Loading for Enhanced Electrocatalytic Nitrogen Reduction to Ammonia, *Small*, 2022, **18**(25), 2200996, DOI: **10.1002/smll.202200996**.

45 D. Zhang, H. Zhao, X. Wu, Y. Deng, Z. Wang, Y. Han, H. Li, Y. Shi, X. Chen, S. Li, J. Lai, B. Huang and L. Wang, Multi-Site Electrocatalysts Boost PH-Universal Nitrogen Reduction by High-Entropy Alloys, *Adv. Funct. Mater.*, 2021, **31**(9), 2006939, DOI: **10.1002/adfm.202006939**.

46 Y. Zhao, F. Li, W. Li, Y. Li, C. Liu, Z. Zhao, Y. Shan, Y. Ji and L. Sun, Identification of M-NH_2-NH_2 Intermediate and

Rate Determining Step for Nitrogen Reduction with Bioinspired Sulfur-Bonded FeW Catalyst, *Angew. Chem., Int. Ed.*, 2021, **60**(37), 20331–20341, DOI: **10.1002/anie.202104918**.

47 D. K. Yesudoss, H. Chun, B. Han and S. Shanmugam, Accelerated N_2 Reduction Kinetics in Hybrid Interfaces of $NbTiO_4$ and Nitrogen-Doped Carbon Nanorod via Synergistic Electronic Coupling Effect, *Appl. Catal., B*, 2022, **304**, 120938, DOI: **10.1016/j.apcatb.2021.120938**.

48 Y. Zhang, Q. Zhang, D.-X. Liu, Z. Wen, J.-X. Yao, M.-M. Shi, Y.-F. Zhu, J.-M. Yan and Q. Jiang, High Spin Polarization Ultrafine Rh Nanoparticles on CNT for Efficient Electrochemical N_2 Fixation to Ammonia, *Appl. Catal., B*, 2021, **298**, 120592, DOI: **10.1016/j.apcatb.2021.120592**.

49 H. He, Q.-Q. Zhu, Y. Yan, H.-W. Zhang, Z.-Y. Han, H. Sun, J. Chen, C.-P. Li, Z. Zhang and M. Du, Metal–Organic Framework Supported Au Nanoparticles with Organosilicone Coating for High-Efficiency Electrocatalytic N_2 Reduction to NH_3, *Appl. Catal., B*, 2022, **302**, 120840, DOI: **10.1016/j.apcatb.2021.120840**.

50 R. Amrine, M. A. Montiel, V. Montiel and J. Solla-Gullón, Evaluation of Pt–Rh Nanoparticle–Based Electrodes for the Electrochemical Reduction of Nitrogen to Ammonia, *Electrocatalysis*, 2024, **15**(2–3), 239–250, DOI: **10.1007/s12678-024-00870-1**.

51 X. Chen, J. Zhou, W. Hu, B. Huang and D. Yuan, Highly Efficient Ru-Based Heusler Alloys for Nitrogen Reduction Reaction: Breaking Scaling Relations and Regulating Potential Determining Steps, *Appl. Surf. Sci.*, 2024, **655**, 159686, DOI: **10.1016/j.apsusc.2024.159686**.

52 Y. Jeong, G. Janani, D. Kim, T.-Y. An, S. Surendran, H. Lee, D. J. Moon, J. Y. Kim, M.-K. Han and U. Sim, Roles of Heterojunction and Cu Vacancies in the Au@$Cu_{2-x}Se$ for the Enhancement of Electrochemical Nitrogen Reduction Performance, *ACS Appl. Mater. Interfaces*, 2023, **15**, 52342–52357, DOI: **10.1021/acsami.3c07947**.

53 T. An, C. Xia, M. Je, H. Lee, S. Ji, M. Kim, S. Surendran, M. Han, J. Lim, D. Lee, J. Y. Kim, T. Kim, H. Choi, J. K. Kim and U. Sim, V_2O_3/VN Electrocatalysts with Coherent Heterogeneous Interfaces for Selecting Low-energy Nitrogen Reduction Pathways, *SusMat*, 2024, **4**(4), 1–14, DOI: **10.1002/sus2.226**.

54 Y. Abghoui, A. L. Garden, J. G. Howalt, T. Vegge and E. Skúlason, Electroreduction of N_2 to Ammonia at Ambient Conditions on Mononitrides of Zr, Nb, Cr, and V: A DFT Guide for Experiments, *ACS Catal.*, 2016, **6**(2), 635–646, DOI: **10.1021/acscatal.5b01918**.

55 B. Han, H. Meng, F. Li and J. Zhao, Fe_3 Cluster Anchored on the C_2N Monolayer for Efficient Electrochemical Nitrogen Fixation, *Catalysts*, 2020, **10**(9), 1–9, DOI: **10.3390/catal10090974**.

56 Y.-Z. Zhang, P.-H. Li, Y.-N. Ren, Y. He, C.-X. Zhang, J. Hu, X.-Q. Cao and M. Leung, Metal-Based Electrocatalysts for Selective Electrochemical Nitrogen Reduction to Ammonia, *Nanomaterials*, 2023, **13**(18), 2580, DOI: **10.3390/nano13182580**.

57 S. Zhang, X. Zhang, C. Liu, L. Pan, C. Shi, X. Zhang, Z. F. Huang and J. J. Zou, Theoretical and Experimental Progress of Metal Electrocatalysts for the Nitrogen Reduction Reaction, *Mater. Chem. Front.*, 2022, **7**(4), 643–661, DOI: **10.1039/d2qm01061e**.

58 E. Skúlason, T. Bligaard, S. Gudmundsdóttir, F. Studt, J. Rossmeisl, F. Abild-Pedersen, T. Vegge, H. Jónsson and J. K. Nørskov, A Theoretical Evaluation of Possible Transition Metal Electro-Catalysts for N_2 Reduction, *Phys. Chem. Chem. Phys.*, 2012, **14**(3), 1235–1245, DOI: **10.1039/c1cp22271f**.

59 S. Wang, C. Qian and S. Zhou, Accelerating the Development of Electrocatalysts for Electrochemical Nitrogen Fixation through Theoretical and Computational Approaches, *Mater. Chem. Front.*, 2023, **7**(19), 4259–4280, DOI: **10.1039/d3qm00267e**.

60 J. G. Howalt, T. Bligaard, J. Rossmeisl and T. Vegge, DFT Based Study of Transition Metal Nano-Clusters for Electrochemical NH_3 Production, *Phys. Chem. Chem. Phys.*, 2013, **15**(20), 7785–7795, DOI: **10.1039/c3cp44641g**.

61 D. Roy, A. Navarro-Vazquez, P. V. R. Schleyer, S. Das, S. Pal and S. Krishnamurty, Modeling Dinitrogen Activation by Lithium: A Mechanistic Investigation of the Cleavage of N_2 by Stepwise Insertion into Small Lithium Clusters, *J. Phys. Chem. C*, 2009, **131**(36), 13045–13053, DOI: **10.1021/ja902980j**.

62 S. Das, S. Pal and S. Krishnamurty, Dinitrogen Activation by Silicon and Phosphorus Doped Aluminum Clusters, *J. Phys. Chem. C*, 2014, **118**(34), 19869–19878, DOI: **10.1021/jp505700a**.

63 M. Jäger, R. Schäfer and R. L. Johnston, GIGA: A Versatile Genetic Algorithm for Free and Supported Clusters and Nanoparticles in the Presence of Ligands, *Nanoscale*, 2019, **11**(18), 9042–9052, DOI: **10.1039/c9nr02031d**.

64 J. B. A. Davis, A. Shayeghi, S. L. Horswell and R. L. Johnston, The Birmingham Parallel Genetic Algorithm and Its Application to the Direct DFT Global Optimisation of Ir_N (N = 10–20) Clusters, *Nanoscale*, 2015, **7**(33), 14032–14038, DOI: **10.1039/C5NR03774C**.

65 M. Jäger, R. Schäfer and R. L. Johnston, First Principles Global Optimization of Metal Clusters and Nanoalloys, *Adv. Phys. X*, 2018, **3**(1), 1077–1108, DOI: **10.1080/23746149.2018.1516514**.

66 R. L. Johnston, Evolving Better Nanoparticles: Genetic Algorithms for Optimising Cluster Geometries, *J. Chem. Soc., Dalton Trans.*, 2003, **3**(22), 4193–4207, DOI: **10.1039/b305686d**.

67 D. M. Deaven and K. M. Ho, Molecular Geometry Optimization with a Genetic Algorithm, *Phys. Rev. Lett.*, 1995, **75**(2), 288–291, DOI: **10.1103/PhysRevLett.75.288**.

68 G. Kresse and J. Hafner, Ab Initio Molecular Dynamics for Liquid Metals, *Phys. Rev. B: Condens. Matter Mater. Phys.*, 1993, **47**(1), 558–561, DOI: **10.1103/PhysRevB.47.558**.

69 G. Kresse and J. Furthmüller, Efficiency of Ab-Initio Total Energy Calculations for Metals and Semiconductors Using a Plane-Wave Basis Set, *Comput. Mater. Sci.*, 1996, **6**(1), 15–50, DOI: **10.1016/0927-0256(96)00008-0**.

70 G. Kresse and J. Hafner, Ab Initio Molecular-Dynamics Simulation of the Liquid–Metalamorphous–Semiconductor

Transition in Germanium, *Phys. Rev. B: Condens. Matter Mater. Phys.*, 1994, **49**(20), 14251–14269, DOI: 10.1103/PhysRevB.49.14251.

71 G. Kresse and J. Furthmüller, Efficient Iterative Schemes for Ab Initio Total-Energy Calculations Using a Plane-Wave Basis Set, *Phys. Rev. B: Condens. Matter Mater. Phys.*, 1996, **54**(16), 11169–11186, DOI: 10.1103/PhysRevB.54.11169.

72 J. P. Perdew, K. Burke and M. Ernzerhof, Generalized Gradient Approximation Made Simple, *Phys. Rev. Lett.*, 1996, **77**(18), 3865–3868, DOI: 10.1103/PhysRevLett.77.3865.

73 G. Kresse and D. Joubert, From Ultrasoft Pseudopotentials to the Projector Augmented-Wave Method, *Phys. Rev. B: Condens. Matter Mater. Phys.*, 1999, **59**(3), 1758–1775, DOI: 10.1103/PhysRevB.59.1758.

74 M. Methfessel and A. T. Paxton, High-Precision Sampling for Brillouin-Zone Integration in Metals, *Phys. Rev. B: Condens. Matter Mater. Phys.*, 1989, **40**(6), 3616–3621, DOI: 10.1103/PhysRevB.40.3616.

75 S. Grimme, S. Ehrlich and L. Goerigk, Effect of the Damping Function in Dispersion Corrected Density Functional Theory, *J. Comput. Chem.*, 2011, **32**(7), 1456–1465, DOI: 10.1002/JCC.21759.

76 S. Grimme, J. Antony, S. Ehrlich and H. Krieg, A Consistent and Accurate Ab Initio Parametrization of Density Functional Dispersion Correction (DFT-D) for the 94 Elements H-Pu, *J. Chem. Phys.*, 2010, **132**(15), 154104, DOI: 10.1063/1.3382344.

77 W. Tang, E. Sanville and G. Henkelman, A Grid-Based Bader Analysis Algorithm without Lattice Bias, *J. Phys.: Condens. Matter*, 2009, **21**(8), 84204, DOI: 10.1088/0953-8984/21/8/084204.

78 V. Wang, N. Xu, J. C. Liu, G. Tang and W. T. Geng, VASPKIT: A User-Friendly Interface Facilitating High-Throughput Computing and Analysis Using VASP Code, *Comput. Phys. Commun.*, 2021, **267**, 108033, DOI: 10.1016/J.CPC.2021.108033.

79 A. A. Peterson, F. Abild-Pedersen, F. Studt, J. Rossmeisl and J. K. Nørskov, How Copper Catalyzes the Electroreduction of Carbon Dioxide into Hydrocarbon Fuels, *Energy Environ. Sci.*, 2010, **3**(9), 1311–1315, DOI: 10.1039/c0ee00071j.

80 J. K. Nørskov, J. Rossmeisl, A. Logadottir, L. Lindqvist, J. R. Kitchin, T. Bligaard and H. Jónsson, Origin of the Overpotential for Oxygen Reduction at a Fuel-Cell Cathode, *J. Phys. Chem. B*, 2004, **108**(46), 17886, DOI: 10.1021/jp047349j.

81 E. Skúlason, T. Bligaard, S. Gudmundsdóttir, F. Studt, J. Rossmeisl, F. Abild-Pedersen, T. Vegge, H. Jónsson and J. K. Nørskov, A Theoretical Evaluation of Possible Transition Metal Electro-Catalysts for N_2 Reduction, *Phys. Chem. Chem. Phys.*, 2012, **14**(3), 1235–1245, DOI: 10.1039/c1cp22271f.

82 R. K. Raju, P. Rodriguez and E. N. Brothers, Electrocatalytic Reduction of CO_2 on Size-Selected Nanoclusters of First-Row Transition Metal Nanoclusters: A Comprehensive Mechanistic Investigation, *Phys. Chem. Chem. Phys.*, 2023, **25**(16), 11630–11652, DOI: 10.1039/d3cp00739a.

83 O. V. Lushchikova, D. M. M. Huitema, P. López-Tarifa, L. Visscher, Z. Jamshidi and J. M. Bakker, Structures of Cu N^+ (n = 3–10) Clusters Obtained by Infrared Action Spectroscopy, *J. Phys. Chem. Lett.*, 2019, **10**(9), 2151–2155, DOI: 10.1021/acs.jpclett.9b00539.

84 G. L. Gutsev, M. D. Mochena, C. W. Bauschlicher, W. J. Zheng, O. C. Thomas and K. H. Bowen, Electronic and Geometrical Structure of Mn_{13} Anions, Cations, and Neutrals, *J. Chem. Phys.*, 2008, **129**(4), 1–6, DOI: 10.1063/1.2956494.

85 P. Bobadova-Parvanova, K. A. Jackson, S. Srinivas and M. Horoi, Structure, Bonding, and Magnetism in Manganese Clusters, *J. Chem. Phys.*, 2005, **122**, 014310, DOI: 10.1063/1.1829048.

86 A. Granja-Delrío, H. A. Abdulhussein and R. L. Johnston, DFT-Based Global Optimization of Sub-Nanometer Ni–Pd Clusters, *J. Phys. Chem. C*, 2019, **123**(43), 26583–26596, DOI: 10.1021/acs.jpcc.9b05970.

87 A. Alvarez-Garcia, E. Flórez, A. Moreno and C. Jimenez-Orozco, CO_2 Activation on Small Cu–Ni and Cu–Pd Bimetallic Clusters, *Mol. Catal.*, 2019, **484**, 110733, DOI: 10.1016/j.mcat.2019.110733.

88 R. V. de Amorim, K. E. A. Batista, G. R. Nagurniak, R. P. Orenha, R. L. T. Parreira and M. J. Piotrowski, CO, NO, and SO Adsorption on Ni Nanoclusters: A DFT Investigation, *Dalton Trans.*, 2020, **49**(19), 6407–6417, DOI: 10.1039/d0dt00288g.

89 K. E. A. Batista, V. K. Ocampo-Restrepo, M. D. Soares, M. G. Quiles, M. J. Piotrowski and J. L. F. Da Silva, Ab Initio Investigation of CO_2 Adsorption on 13-Atom 4d Clusters, *J. Chem. Inf. Model.*, 2020, **60**(2), 537–545, DOI: 10.1021/acs.jcim.9b00792.

90 J. Meng, Large Adsorption Energies for CO on Sc_n (n = 2–8, 13) Nanoclusters, *Chin. Phys. B*, 2016, **25**, 123601, DOI: 10.1088/1674-1056/25/12/123601.

91 J. Meyer, M. Tombers, C. Van Wüllen, G. Niedner-Schatteburg, S. Peredkov, W. Eberhardt, M. Neeb, S. Palutke, M. Martins and W. Wurth, The Spin and Orbital Contributions to the Total Magnetic Moments of Free Fe, Co, and Ni Clusters, *J. Chem. Phys.*, 2015, **143**, 104302, DOI: 10.1063/1.4929482.

92 J. Meng, Large Adsorption Energies for CO on Sc_n (n = 2–8, 13) Nanoclusters, *Chin. Phys. B*, 2016, **25**, 123601, DOI: 10.1088/1674-1056/25/12/123601.

93 J. Wang, Structural, Electronic, and Magnetic Properties of Sc_n (N = 2–18) Clusters from Density Functional Calculations, *Phys. Rev. B: Condens. Matter Mater. Phys.*, 2007, **75**(15), 1–9, DOI: 10.1103/PhysRevB.75.155422.

94 H. K. Yuan, H. Chen, A. S. Ahmed and J. F. Zhang, Density-Functional Study of Sc_n (N = 2–16) Clusters: Lowest-Energy Structures, Electronic Structure, and Magnetism, *Phys. Rev. B: Condens. Matter Mater. Phys.*, 2006, **74**(14), 1–12, DOI: 10.1103/PhysRevB.74.144434.

95 X. J. Feng, T. T. Cao, L. X. Zhao, Y. M. Lei and Y. Luo, Structural and Electronic Properties of Re_n ($n \leq 8$) Clusters by Density-Functional Theory, *Eur. Phys. J. D*, 2008, **50**(3), 285–288, DOI: 10.1140/epjd/e2008-00231-y.

96 W. X. Ji, C. W. Zhang, F. Li, P. Li, P. J. Wang, M. J. Ren and M. Yuan, First-Principles Study of Small Pd–Au Alloy Clusters on Graphene, *RSC Adv.*, 2014, **4**(99), 55781–55789, DOI: **10.1039/c4ra07996e**.

97 H. K. Yuan, H. Chen, A. L. Kuang, C. L. Tian and J. Z. Wang, The Spin and Orbital Moment of Fe_n (n = 2–20) Clusters, *J. Chem. Phys.*, 2013, **139**, 034314, DOI: **10.1063/1.4813611**.

98 A. Taneda, T. Shimizu and Y. Kawazoe, Stable Disordered Structures of Vanadium Clusters, *J. Phys.: Condens. Matter*, 2001, **13**, L305, DOI: **10.1088/0953-8984/13/16/101**.

99 S. Li, M. M. G. Alemany and J. R. Chelikowsky, Ab Initio Calculations for the Photoelectron Spectra of Vanadium Clusters, *J. Chem. Phys.*, 2004, **121**(12), 5893–5898, DOI: **10.1063/1.1785142**.

100 C. Ratsch, A. Fielicke, A. Kirilyuk, J. Behler, G. Von Helden, G. Meijer and M. Scheffler, Structure Determination of Small Vanadium Clusters by Density-Functional Theory in Comparison with Experimental Far-Infrared Spectra, *J. Chem. Phys.*, 2005, **122**(12), 1–15, DOI: **10.1063/1.1862621**.

101 F. Baletto, Structural Properties of Sub-Nanometer Metallic Clusters, *J. Phys.: Condens. Matter*, 2019, **31**, 113001, DOI: **10.1088/1361-648X/aaf989**.

102 J. Jellinek, P. H. Acioli, J. Garciá-Rodeja, W. Zheng, O. C. Thomas and K. H. Bowen, Mnn-Clusters: Size-Induced Transition to Half Metallicity, *Phys. Rev. B: Condens. Matter Mater. Phys.*, 2006, **74**(15), 1–4, DOI: **10.1103/PhysRevB.74.153401**.

103 D. Die, B. X. Zheng, L. Q. Zhao, Q. W. Zhu and Z. Q. Zhao, Insights into the Structural, Electronic and Magnetic Properties of V-Doped Copper Clusters: Comparison with Pure Copper Clusters, *Sci. Rep.*, 2016, **6**, 1–13, DOI: **10.1038/srep31978**.

104 C. G. Li, Z. G. Shen, Y. F. Hu, Y. N. Tang, W. G. Chen and B. Z. Ren, Insights into the Structures and Electronic Properties of $Cu_n + 1\mu$ and Cu_nS_μ (n = 1–12; μ = 0, ±1) Clusters, *Sci. Rep.*, 2017, **7**(1), 1–11, DOI: **10.1038/s41598-017-01444-6**.

105 T. Wang, B. Li, H. Liu, X. Zhang, R. K. Hocking and C. Sun, First Principles Study of Single Fe Atom Supported on TiO_2(0 0 1) for Nitrogen Reduction to Ammonia, *Appl. Surf. Sci.*, 2022, **572**, 151417, DOI: **10.1016/j.apsusc.2021.151417**.

106 Q. Li, S. Qiu, M. Yan, C. Liu, F. Zhou, B. Jia, L. He, X. Zhang and C. Sun, Insight into the Reactivity of Carbon Structures for Nitrogen Reduction Reaction, *Langmuir*, 2021, **37**(50), 14657–14667, DOI: **10.1021/acs.langmuir.1c02358**.

107 A. Rasool and M. A. Dar, Multistep Screening of Transition-Metal-Based Homonuclear Double-Atom Catalysts to Unravel the Electronic Origin of Their Activity and Selectivity Challenges for Nitrogen Reduction, *Catal. Sci. Technol.*, 2024, **14**, 5687–5698, DOI: **10.1039/d4cy00480a**.

108 S. Chen, Y. Gao, W. Wang, O. V. Prezhdo and L. Xu, Prediction of Three-Metal Cluster Catalysts on Two-Dimensional W_2N_3 Support with Integrated Descriptors for Electrocatalytic Nitrogen Reduction, *ACS Nano*, 2023, **17**(2), 1522–1532, DOI: **10.1021/acsnano.2c10607**.

109 H. Yang, D. Luo, R. Gao, D. Wang, H. Li, Z. Zhao, M. Feng and Z. Chen, Reduction of N_2 to NH_3 by TiO_2-Supported Ni Cluster Catalysts: A DFT Study, *Phys. Chem. Chem. Phys.*, 2021, **23**(31), 16707–16717, DOI: **10.1039/d1cp00859e**.

110 A. Rasool, I. Anis, S. A. Bhat and M. A. Dar, Optimizing the NRR Activity of Single and Double Boron Atom Catalysts Using a Suitable Support: A First Principles Investigation, *Phys. Chem. Chem. Phys.*, 2023, **25**(33), 22275–22285, DOI: **10.1039/d3cp02358c**.

111 M. I. Ahmed, L. J. Arachchige, Z. Su, D. B. Hibbert, C. Sun and C. Zhao, Nitrogenase-Inspired Atomically Dispersed Fe–S–C Linkages for Improved Electrochemical Reduction of Dinitrogen to Ammonia, *ACS Catal.*, 2022, **12**(2), 1443–1451, DOI: **10.1021/acscatal.1c05174**.

112 Q. Li, S. Qiu, C. Liu, M. Liu, L. He, X. Zhang and C. Sun, Computational Design of Single-Molybdenum Catalysts for the Nitrogen Reduction Reaction, *J. Phys. Chem. C*, 2019, **123**(4), 2347–2352, DOI: **10.1021/acs.jpcc.8b11509**.

113 A. Das, S. Das and B. Pathak, The Electrocatalytic N_2 Reduction Activity of Core-Shell Iron Nanoalloy Catalysts: A Density Functional Theory (DFT) Study, *Phys. Chem. Chem. Phys.*, 2023, **25**(48), 32913–32921, DOI: **10.1039/d3cp03453d**.

114 I. Anis, S. Amin, G. M. Rather and M. A. Dar, N_2 Activation and Reduction on Graphdiyne Supported Single, Double, and Triple Boron Atom Catalysts: A First Principles Investigation, *ChemistrySelect*, 2023, **8**, e202300993, DOI: **10.1002/slct.202300993**.

115 N. Li, Z. Wang, P. Zhang, X. Li, A. Arramel, C. Sun, X. Zhou and X. Zhao, Regulating the Spin Order of Transition Metal Embedded-MXenes for Boosting Electrocatalytic Nitrogen Reduction to Ammonia, *J. Mater. Chem. A*, 2022, **10**(42), 22760–22770, DOI: **10.1039/d2ta06151a**.

